

A time step-size computing arc-length method for the phase-field hydraulic fracture model

Bharali, Ritukesh; van der Meer, Frans P.; Larsson, Fredrik; Jänicke, Ralf

DOI

[10.1016/j.cma.2024.117687](https://doi.org/10.1016/j.cma.2024.117687)

Publication date

2025

Document Version

Final published version

Published in

Computer Methods in Applied Mechanics and Engineering

Citation (APA)

Bharali, R., van der Meer, F. P., Larsson, F., & Jänicke, R. (2025). A time step-size computing arc-length method for the phase-field hydraulic fracture model. *Computer Methods in Applied Mechanics and Engineering*, 436, Article 117687. <https://doi.org/10.1016/j.cma.2024.117687>

Important note

To cite this publication, please use the final published version (if applicable). Please check the document version above.

Copyright

Other than for strictly personal use, it is not permitted to download, forward or distribute the text or part of it, without the consent of the author(s) and/or copyright holder(s), unless the work is under an open content license such as Creative Commons.

Takedown policy

Please contact us and provide details if you believe this document breaches copyrights. We will remove access to the work immediately and investigate your claim.

Contents lists available at [ScienceDirect](https://www.sciencedirect.com)

Comput. Methods Appl. Mech. Engrg.

journal homepage: www.elsevier.com/locate/cma

A time step-size computing arc-length method for the phase-field hydraulic fracture model

 Ritukesh Bharali ^a,* , Frans P. van der Meer ^b, Fredrik Larsson ^a, Ralf Jänicke ^c
^a Department of Industrial and Material Science, Chalmers University of Technology, Sweden

^b Faculty of Civil Engineering and Geosciences, Delft University of Technology, The Netherlands

^c Institute of Applied Mechanics, Technische Universität Braunschweig, Germany

ARTICLE INFO

Keywords:

 Arc-length
 Adaptive time-step
 Hydraulic fracture
 Phase-field fracture

ABSTRACT

The phase-field hydraulic fracture model entails a non-convex energy functional. This renders a poor convergence behaviour for monolithic solution techniques, such as the Newton–Raphson method. Consequently, researchers have adopted alternative solution techniques such as the staggered solution technique and the Newton–Raphson method with convexification via extrapolation of the phase-field. Both methods are robust. However, the former is computationally expensive and in the latter, the extrapolation itself is questionable w.r.t regularity in time. In this work, a novel dissipation-based arc-length method is proposed as a robust and computationally efficient monolithic solution technique for the phase-field hydraulic fracture model. Similar to brittle fracture in force driven mechanical problems, constant flux driven hydraulic fracture processes are also unstable. Furthermore, due to the constant flux loading in hydraulic fracturing problems, scaling of the external force is not possible. Instead, the time step-size is considered as the additional unknown, augmenting the arc-length constraint equation. The robustness and computational efficiency of the proposed arc-length method is demonstrated using numerical experiments, where comparisons are made with the staggered solver as well as the quasi-Newton BFGS method.

1. Introduction

The computational modelling of fluid-driven fracture is imperative for reliable hydraulic fracturing operations. The applications of such operations are diverse, ranging from extraction of petroleum and natural gas, via geothermal energy production, to the geological storage of carbon dioxide. This motivates the need for accurate computational models describing the fluid-driven fracturing phenomenon.

The computational modelling of the fracturing process using the conventional Finite Element Method [1–3] is not possible on a fixed mesh. Therefore, Secchi, Simoni, and Schrefler introduced re-meshing techniques for modelling hydraulic fracture (fracking) in [4,5]. Later, the development of the eXtended Finite Element Method (XFEM) [6,7] enabled the augmentation of the displacement spaces with special enrichment functions capable of reproducing discontinuous and singular elastic fields associated with fractures. These enrichment functions are dynamically incorporated into the computational model as the fracture propagates. The early adaptation of the XFEM towards hydraulic fracturing was carried out by Gordeliy and Peirce in [8–10]. Later studies extended the model to a three-dimensional framework [11], anisotropic modelling of the shale reservoir [12], interaction of new fractures with existing natural fractures [13], and investigations into the fracture/pore mass exchange [14] to cite a few. Adopting an alternative

* Corresponding author.

E-mail address: ritukesh.bharali@chalmers.se (R. Bharali).

<https://doi.org/10.1016/j.cma.2024.117687>

Received 8 August 2024; Received in revised form 1 December 2024; Accepted 16 December 2024

Available online 31 December 2024

0045-7825/© 2024 The Authors. Published by Elsevier B.V. This is an open access article under the CC BY license (<http://creativecommons.org/licenses/by/4.0/>).

approach, the Cohesive Zone Model (CZM) [15–17] was used to model hydraulic fracturing in [18–20]. The XFEM and CZM hydraulic fracturing models inherit the computational challenges associated with discrete fracture models, viz., the need for a fracture tracking algorithm, re-meshing, and dynamic insertion of enriched shape functions/cohesive elements. For topologically complex fracturing phenomenon (such as, branching, kinking and merging of fractures), the aforementioned computational challenges may be prohibitively tedious.

The tedious aspects of the discrete fracture modelling techniques (XFEM, CZM) are circumvented by the phase-field fracture model [21]. The phase-field fracture model [22–24] belongs to the smeared (diffused) representation of fracture, and is based on the comparatively simple notion of energy minimization. Complex fracture topologies are simulated based on this minimization without the need for any *ad hoc* criterion or fracture tracking algorithm. As such, the phase-field fracture model has been adopted in a variety of engineering problems, including hydraulic fracturing. The pioneering works in phase-field hydraulic fracturing model was carried out by Mikelić, Wheeler, Wick, and Wollner [25–28], and Bourdin, Chukwudozie, and Yoshioka [29–31]. In the same period and later, several variants [32–39] have been proposed, largely differing in the construction of the poroelastic energy functional and in the delineation of the bulk reservoir and fracture domains.

In the context of the poroelastic phase-field energy functional construct, there is a lack of consensus w.r.t. the degradation of the fluid pressure contribution. Zhou et al. [36], and Heider and Sun [37] proposed that the phase-field based degradation be applied only on the solid skeleton and not on the fluid pressure contribution. The authors instead advocated for the degradation of the fluid pressure contribution for soil desiccation problems, a choice later supported by analytical studies in Luo et al. [40]. However, in several other hydraulic fracturing works [27,38,41], the fluid pressure term was also degraded upon fracture. You and Yoshioka [41] argued that degrading the fluid pressure term maintains the stress continuity across the fracture for all values of the Biot coefficient. However, when the fluid pressure term is not degraded, the stress continuity holds only when the Biot coefficient is unity. In this work, the Biot coefficient is set to one for all problems.

In addition to a suitable poroelastic phase-field energy functional construct, a proper representation of the fluid flow in the bulk reservoir domain and within the fractures is required [32]. The fluid pressure plays a key role in driving solid skeleton deformation and the initiation and propagation of the fracture(s) in a porous medium. In the bulk reservoir domain of rock specimens, the fluid permeates through interconnected pores and is modelled using the Darcy's law. However, upon fracturing, the fluid flow is idealized as flow between parallel plates, transitioning from Darcy to a Poiseuille type flow. Therefore, it is important to delineate the bulk reservoir and the fracture domains. For discrete fracture models like XFEM and CZM, the delineation is present in the computational model by construct. However, in phase-field fracture models, the fracture is represented by a smeared (diffused) localized zone of finite width. This makes the delineation process heuristic, and dependent on a user-defined threshold phase-field value [36,37].

Despite the aforementioned developments in the phase-field hydraulic fracture models, a robust and computationally efficient monolithic solution technique is still elusive, to the best of the authors' knowledge. This is due to the non-convex nature of the underlying energy functional [42]. Mikelić, Wheeler, Wick, and Wollner in [26–28] adopted a convexification strategy whereby the phase-field in the balance of momentum equation was extrapolated from the two previously converged steps [43]. Consequently, the Newton–Raphson method was demonstrated as convergent. However, as stated by the authors themselves, in the absence of regularity of the phase-field in time, the extrapolation technique itself is questionable. Finally, a black-box monolithic solver PANDAS¹ has also been adopted for hydraulic fracturing problems [33,44]. These works do not report any implementation details (line search, iteration terminating tolerances, etc.) and performance measures (iterations to converge, wall time). Departing from the monolithic approach, the staggered solution technique [23,24] was adopted in most other phase-field hydraulic fracturing studies [25,29–31,35–38,41]. Although robust, the staggered solution technique is computationally expensive. The state-of-the-art pertaining to solution techniques for phase-field hydraulic fracturing lacks a robust and computationally efficient monolithic solution technique.

In this work, a novel monolithic solution technique is proposed for phase-field hydraulic fracturing in form of the arc-length method. A dissipation-based arc-length constraint equation is adopted [45]. For linear elastic fracture problems, the robustness and computational efficiency of the arc-length method has been demonstrated in [45–48]. In these problems, the external load is scaled with a scalar load parameter the magnitude of which becomes an additional unknown in the system of equations. However, for phase-field hydraulic fracturing problems, such an approach is not possible as the problems are often driven by a constant flux (an assumption commonly adopted in the literature [25,29–31,35–38,41]). This eliminates the option to use the load scale factor as additional unknown. In this work, instead of scalar load parameter, the time step-size is considered as an additional scalar unknown augmenting the displacement, fluid pressure, and phase-field solution space. The set of discrete equations for solving a hydraulic fracturing problem is presented along with the implementation caveats. The latter include a user criterion for switching from the conventional Newton–Raphson method to the arc-length method based on a threshold energy, and an adaptive modification of the arc-length based on convergence achieved in the previous computation step. The performance of this novel arc-length method construct is assessed on benchmark problems, presented earlier in [27]. Comparisons are made with the quasi-Newton BFGS method and the staggered solver [23,24] w.r.t. average iterations and wall time. Note that the BFGS method has only been used in the context of soil consolidation [49] and not for phase-field hydraulic fracture, to the best of the authors' knowledge.

The article is organized as follows: Section 2 presents the phase-field hydraulic fracturing model (the energy functional and fluid transport equation and their corresponding weak form equations). Subsequently, in Section 3, the discrete problem and the arc-length method are introduced. Section 4 presents the numerical experiments on benchmark hydraulic fracturing problems. Therein, the performance of the arc-length method is carried out w.r.t. the staggered solution technique and the quasi-Newton BFGS method. Finally, Section 5 concludes the article with remarks on the novel arc-length method and an outlook to future works.

¹ PANDAS available to purchase at <https://sciengine.de/index.php> is closed-source and lacks documentation.

2. Phase-field hydraulic fracturing model

The phase-field hydraulic fracturing model comprises of an energy functional accounting for deformation of the solid skeleton and fracture (at fixed fluid pressure) and a transport equation for the fluid pressure. The latter is derived using the conservation of solid and fluid masses [50,51]. Finally, the model is presented within the small strain framework, a choice adopted in most hydraulic fracturing studies in the literature [25–28,31,36–38,41].

2.1. The energy functional

The poro-elastic phase-field fracture energy functional for hydraulic fracturing is an extension of its purely solid phase linear elastic counterpart,

$$\begin{aligned} E_{\text{solid}}(\mathbf{u}, \varphi) = & \int_{\Omega} g(\varphi) \Psi^+(\epsilon[\mathbf{u}]) \, d\Omega + \int_{\Omega} \Psi^-(\epsilon[\mathbf{u}]) \, d\Omega \\ & - \int_{\Gamma_N^u} \mathbf{t}_p^u \cdot \mathbf{u} \, d\Gamma - \int_{\Omega} \mathbf{b} \cdot \mathbf{u} \, d\Omega \\ & + \int_{\Omega} \frac{G_c}{c_w} \left(\frac{w(\varphi)}{l} + l |\nabla \varphi|^2 \right) \, d\Omega, \end{aligned} \quad (1)$$

with pertinent fluid pressure contributions. Prior to that, it is imperative to explain the different terms and coefficients used in the above expression. The strain energy density $\Psi(\epsilon[\mathbf{u}])$ is additively decomposed into a fracture driving part and a residual energy, denoted as $\Psi^+(\epsilon[\mathbf{u}])$ and $\Psi^-(\epsilon[\mathbf{u}])$, respectively. The phase-field based degradation function $g(\varphi)$ acts on the fracture driving strain energy density. In this work, the spectral decomposition-based split proposed by Miehe et al. [52] is adopted. Furthermore, \mathbf{t}_p^u and \mathbf{b} are external traction and body forces. Finally, the last integral of the energy functional represents the fracture energy where, G_c is the Griffith fracture toughness, c_w is a normalization constant associated with the locally dissipated fracture energy function $w(\varphi)$, and l is the fracture length-scale.

The extension of the phase-field fracture energy functional from the purely solid phase linear elastic media to hydraulic fracturing is carried out adapting the seminal work of Biot [53]. The extended energy functional is postulated as a function of the strain $\epsilon[\mathbf{u}]$, the phase-field φ , and the increment of the fluid content ζ . The lattermost is defined as,

$$\zeta = \frac{p}{M} + \alpha \nabla \cdot \mathbf{u}, \quad (2)$$

where, α and M represent the Biot coefficient and Biot modulus, respectively. The energy functional in conjunction with the phase-field fracture is then expressed as,

$$\begin{aligned} E(\mathbf{u}, p, \varphi) = & \int_{\Omega} g(\varphi) \Psi^+(\epsilon[\mathbf{u}]) \, d\Omega + \int_{\Omega} \Psi^-(\epsilon[\mathbf{u}]) \, d\Omega \\ & - \int_{\Omega} \alpha p \nabla \cdot \mathbf{u} \, d\Omega - \int_{\Omega} \frac{p^2}{2M} \, d\Omega - \int_{\Gamma_N^u} \mathbf{t}_p^u \cdot \mathbf{u} \, d\Gamma \\ & - \int_{\Omega} \mathbf{b} \cdot \mathbf{u} \, d\Omega + \int_{\Omega} \frac{G_c}{c_w} \left(\frac{w(\varphi)}{l} + l |\nabla \varphi|^2 \right) \, d\Omega. \end{aligned} \quad (3)$$

In the above expression, a Legendre transformation is carried out to replace the argument ζ with the fluid pressure p . Similar energy functionals may be observed in works of Zhou, Zhuang, and Rabczuk [36,37] and Heider and Sun [37]. In the energy functional (3), the energetic terms associated with the fluid pressure are assumed unaffected by the degradation function $g(\varphi)$. Consequently, the stress continuity across the fracture is ensured only when the Biot coefficient is set to 1 [41].

Remark 1. It is important to note that the fluid pressure p is not computed from the minimization of the energy functional (3). Instead, it is obtained from a transport equation, derived from the conservation of solid skeleton and fluid masses.

2.2. Fluid transport

The transport equation for the fluid in the porous medium is obtained using the conservation of mass for the solid as well as the fluid [50,51]. It is stated as,

$$\underbrace{\left[\frac{\alpha - n}{K_s} + \frac{n}{K_f} \right]}_{\frac{1}{M}} \frac{\partial p}{\partial t} + \alpha \frac{\partial \epsilon_{\text{vol}}}{\partial t} - \nabla \cdot \underbrace{\left[\frac{\kappa_i \mathbf{I}}{\mu_f} \nabla p \right]}_{\mathbf{K}_{\text{eff}}} = 0, \quad (4)$$

where, n refers to the porosity of the specimen, K_s and K_f represent the bulk modulus of the solid grains and the fluid, respectively. The volumetric strain measure $\epsilon_{\text{vol}} := \nabla \cdot \mathbf{u}$, and isotropic permeability second-order tensor (matrix) \mathbf{K}_{eff} is obtained using the intrinsic permeability κ_i and the fluid dynamic viscosity μ_f , respectively. In the absence of fracture dependent coefficients, the fluid transport (4) remains applicable only for poro-elasticity studies. In such a case, the fluid flow in a fractured domain is not correctly represented [32]. In this work, the permeability and the porosity of the porous rock medium are enhanced upon fracture.

The permeability, say \mathbf{K}_f in a fracture is assumed to be function of the fracture aperture, based on Witherspoon et al.'s cubic law [54]. With this assumption, the fluid flow in the fracture is postulated to be of Poiseuille type. The fracture permeability \mathbf{K}_f is then expressed as,

$$\mathbf{K}_f = \frac{w_f^2}{12} \mathbf{I}, \tag{5}$$

where, w_f is the fracture aperture. For phase-field fracture models, however, the fracture aperture is not obtained explicitly as a part of the solution. Instead, it is computed in an approximate fashion [55]. Among the several methods (see Section 3 in [55]), Miehe et al.'s relation [56],

$$w_f := \langle h_{el}(1 + \mathbf{n}_\varphi \cdot \epsilon[\mathbf{u}] \cdot \mathbf{n}_\varphi) \rangle_+, \quad \text{with } \mathbf{n}_\varphi \approx \frac{\nabla\varphi}{|\nabla\varphi|}, \tag{6}$$

is adopted in this work, where h_{el} is the characteristic element size. This relation allows a pointwise computation of the fracture aperture, based on the integration point strain and phase-field gradient. Having established the notion of the fracture permeability \mathbf{K}_f and permeability of the bulk specimen \mathbf{K}_b , the effective permeability \mathbf{K}_{eff} corresponding to a fracturing material state is postulated as,

$$\mathbf{K}_{eff}(\varphi, \epsilon_{vol}[\mathbf{u}]) = \mathbf{K}_b + h(\varphi, \epsilon_{vol}[\mathbf{u}]) (\mathbf{K}_f - \mathbf{K}_b). \tag{7}$$

In the above expression, $h(\varphi, \epsilon_{vol}[\mathbf{u}])$ is an interpolation function defined as,

$$h(\varphi, \epsilon_{vol}[\mathbf{u}]) = \mathcal{H}(\epsilon_{vol}) \left(\frac{\langle \varphi - \varphi_{th} \rangle^+}{\langle 1.0 - \varphi_{th} \rangle} \right)^2, \tag{8}$$

with \mathcal{H} denoting the Heaviside function. The interpolation function assumes a value zero for closed cracks ($\epsilon_{vol}[\mathbf{u}] \leq 0$) and for the phase-field φ less than a user-defined threshold value $\varphi_{th} = 0.8$. In these scenarios, the effective permeability is assumed as the bulk permeability ($\mathbf{K}_{eff} = \mathbf{K}_b$). For open-cracks ($\epsilon_{vol}[\mathbf{u}] > 0$) and $\varphi > \varphi_{th}$, the effective permeability is interpolated between the bulk and fracture values.

Similar to the effective permeability, the porosity of the specimen is also interpolated between bulk and fractured material states. The bulk porosity $n_b \in [0.2, 0.4]$ for rock specimen is defined by the user, while the fracture porosity is assumed as unity [41]. Subsequently, the material state dependent expression for porosity is given by,

$$n(\varphi, \epsilon_{vol}[\mathbf{u}]) = n_b + h(\varphi, \epsilon_{vol}[\mathbf{u}]) (n_f - n_b), \tag{9}$$

Upon incorporating the fracture dependent permeability (7) and porosity (9) in the fluid transport equation (4), one obtains,

$$\underbrace{\left[\frac{\alpha - n(\varphi, \epsilon_{vol})}{K_s} + \frac{n(\varphi, \epsilon_{vol})}{K_f} \right]}_{\frac{1}{M}(\varphi, \epsilon_{vol})} \frac{\partial p}{\partial t} + \alpha \frac{\partial \epsilon_{vol}}{\partial t} - \nabla \cdot \left[\mathbf{K}_{eff}(\varphi, \epsilon_{vol}) \nabla p \right] = 0. \tag{10}$$

2.3. Weak form equations

The set of weak form equations for the phase-field hydraulic fracture model is obtained through a two-fold process. First, the momentum balance and the phase-field evolution equations are obtained through minimization of the energy functional (3), w.r.t., the vector-valued displacement \mathbf{u} and the scalar-valued phase-field φ . Thereafter, the fluid transport weak form equation is obtained upon performing a Backward Euler substitution of the time derivatives and subsequently integrating the strong form (10) with a test function δp over the domain Ω . For the sake of brevity, the function arguments $(\varphi, \epsilon_{vol})$ in \mathbf{K}_{eff} and n are dropped henceforth. Furthermore, the Cauchy effective stress $\sigma[\mathbf{u}] := g(\varphi) \frac{\partial \psi^+[\mathbf{u}]}{\partial \epsilon} + \frac{\partial \psi^-[\mathbf{u}]}{\partial \epsilon}$.

The set of weak form equations for the phase-field hydraulic fracture model in conjunction with appropriate trial and test functions are presented as **Weak form Problem 1**. One may note that the **Weak form Problem 1** is of saddle point nature, where the pressure field acts as a Lagrange multiplier constraining the displacement field. Consequently, a careful choice of trial and test functions is required for the displacement and the water pressure to guarantee a unique solution continuously depending on the input data. The sufficient condition ensuring this uniqueness is established in the computational mechanics literature as the Ladyzhenskaya–Babuška–Brezzi (LBB) condition. In order to fulfil the LBB condition, quadratic trial and test functions are chosen for the displacement field and the phase-field, while the pressure field remains linear. In the discrete sense, such a choice is referred to as the **Taylor and Hood** element following their contribution [57]. Note that one may adopt lower order elements with stabilization techniques, e.g., Finite Increment Calculus (FIC) [58], Fluid Pressure Laplacian (FPL) [59,60], Polynomial Pressure Projection (PPP) [61], or assumed strain finite element formulation [62,63]. Most of these techniques, however, perform adequately for poroelastic problems, and their extension towards problems involving damage or fracture is not straight-forward. Gavagnin et al. adopted the PPP approach for poroelastic problems exhibiting deviatoric fracturing phenomenon [64].

Weak form Problem 1. Find $(\mathbf{u}, \varphi, p) \in \mathbb{U} \times \mathbb{P} \times \mathbb{Q}$ such that

$$E'(\mathbf{u}, p, \varphi; \delta \mathbf{u}) = \int_{\Omega} \left(g(\varphi) \sigma^+[\mathbf{u}] + \sigma^-[\mathbf{u}] \right) : \epsilon[\delta \mathbf{u}] \, d\Omega$$

$$- \int_{\Omega} \alpha p \mathbf{I} : \epsilon[\delta \mathbf{u}] \, d\Omega = 0 \quad \forall \delta \mathbf{u} \in \mathbb{U}^0, \quad (11a)$$

$$E'(\mathbf{u}, p, \varphi; \hat{\varphi}) = \int_{\Omega} \left(g'(\varphi) \Psi^+(\epsilon[\mathbf{u}]) + \frac{G_c}{c_w l} w'(\varphi) \right) (\hat{\varphi} - \varphi) \, d\Omega \\ + \int_{\Omega} \frac{G_c l}{c_w} \nabla \varphi \cdot \nabla (\hat{\varphi} - \varphi) \, d\Omega \geq 0 \quad \forall \hat{\varphi} \in \mathbb{P}, \quad (11b)$$

$$\int_{\Omega} \left(\frac{1}{M} \frac{p - {}^n p}{\Delta t} + \alpha \frac{\epsilon_{\text{vol}} - {}^n \epsilon_{\text{vol}}}{\Delta t} \right) \delta p \, d\Omega \\ + \int_{\Omega} \nabla \delta p \mathbf{K}_{\text{eff}} \nabla p \, d\Omega \\ = \int_{\Gamma_N^p} q \delta p \, d\Gamma \quad \forall \delta p \in \mathbb{Q}, \quad (11c)$$

using pertinent time-dependent Dirichlet boundary conditions \mathbf{u}^p on Γ_D^u , φ^p on Γ_D^φ and p^p on Γ_D^p , and Neumann boundary condition q on Γ_N^p . The trial and test spaces are defined as

$$\mathbb{U} = \{\mathbf{u} \in [H^2(\Omega)]^{\text{dim}} \mid \mathbf{u} = \mathbf{u}^p \text{ on } \Gamma_D^u\}, \quad (12a)$$

$$\mathbb{P} = \{\varphi \in [H^2(\Omega)] \mid \varphi \geq {}^n \varphi \mid \varphi = \varphi^p \text{ on } \Gamma_D^\varphi\}, \quad (12b)$$

$$\mathbb{Q} = \{p \in H^1(\Omega) \mid p = p^p \text{ on } \Gamma_D^p\}, \quad (12c)$$

$$\mathbb{U}^0 = \{\mathbf{u} \in [H^2(\Omega)]^{\text{dim}} \mid \mathbf{u} = \mathbf{0} \text{ on } \Gamma_D^u\}, \quad (12d)$$

$$\mathbb{Q}^0 = \{p \in H^1(\Omega) \mid p = 0 \text{ on } \Gamma_D^p\}. \quad (12e)$$

In (12b), the left superscript n refers to the previous time-step. ■

In **Weak form Problem 1**, the notion of irreversible fracture $\dot{\varphi} \geq 0$ manifests in the form of a variational inequality phase-field evolution Eq. (11b) with a restricted trial/test space (12c). However, the Finite Element Method (FEM) does not support in the implementation of such restrictive trial/test spaces. Therefore, the variational inequality is transformed into an ‘equivalent’ equality formulation using the history variable approach, proposed by Miehe et al. [65]. The history variable approach stores the maximum value of the fracture driving energy $\Psi^+(\epsilon[\mathbf{u}])$ in an implicit ‘history variable’ \mathbb{H} . Thereafter, $\Psi^+(\epsilon[\mathbf{u}])$ in (11b) is replaced by \mathbb{H} , resulting in an equality formulation. Mathematically, \mathbb{H} is defined as

$$\mathbb{H} = \max\{{}^n \mathbb{H}, \Psi^+(\epsilon[\mathbf{u}])\} \quad (13)$$

where n refers to the previous time-step. Incorporating \mathbb{H} in (11b) transforms the **Weak form Problem 1** into an alternative, equality-based **Weak form Problem 2**.

Weak form Problem 2. Find $(\mathbf{u}, \varphi, p) \in \mathbb{U} \times \mathbb{P} \times \mathbb{Q}$ such that

$$E'(\mathbf{u}, p, \varphi; \delta \mathbf{u}) = \int_{\Omega} \left(g(\varphi) \sigma^+[\mathbf{u}] + \sigma^-[\mathbf{u}] \right) : \epsilon[\delta \mathbf{u}] \, d\Omega \\ - \int_{\Omega} \alpha p \mathbf{I} : \epsilon[\delta \mathbf{u}] \, d\Omega = 0 \quad \forall \delta \mathbf{u} \in \mathbb{U}^0, \quad (14a)$$

$$E'(\mathbf{u}, p, \varphi; \delta \varphi) = \int_{\Omega} \left(g'(\varphi) \mathbb{H} + \frac{G_c}{c_w l} w'(\varphi) \right) \delta \varphi \, d\Omega \\ + \int_{\Omega} \frac{G_c l}{c_w} \nabla \varphi \cdot \nabla \delta \varphi \, d\Omega = 0 \quad \forall \delta \varphi \in \mathbb{P}^0, \quad (14b)$$

$$\int_{\Omega} \left(\frac{1}{M} \frac{p - {}^n p}{\Delta t} + \alpha \frac{\epsilon_{\text{vol}} - {}^n \epsilon_{\text{vol}}}{\Delta t} \right) \delta p \, d\Omega \\ + \int_{\Omega} \nabla \delta p \mathbf{K}_{\text{eff}} \nabla p \, d\Omega \\ = \int_{\Gamma_N^p} q \delta p \, d\Gamma \quad \forall \delta p \in \mathbb{Q}, \quad (14c)$$

using pertinent time-dependent Dirichlet boundary conditions \mathbf{u}^p on Γ_D^u and φ^p on Γ_D^φ , and Neumann boundary condition t_p^u on Γ_N^u . The superscript n in the above equation indicates the previous (pseudo) time-step. The trial and test spaces are defined as

$$\mathbb{U} = \{\mathbf{u} \in [H^2(\Omega)]^{\text{dim}} \mid \mathbf{u} = \mathbf{u}^p \text{ on } \Gamma_D^u\}, \quad (15a)$$

$$\mathbb{P} = \{\varphi \in [H^2(\Omega)] \mid \varphi = \varphi^p \text{ on } \Gamma_D^\varphi\}, \quad (15b)$$

$$\mathbb{Q} = \{p \in H^1(\Omega) \mid p = p^p \text{ on } \Gamma_D^p\}, \quad (15c)$$

$$\mathbb{U}^0 = \{\mathbf{u} \in [H^2(\Omega)]^{\text{dim}} \mid \mathbf{u} = \mathbf{0} \text{ on } \Gamma_D^u\}, \quad (15d)$$

$$\mathbb{P}^0 = \{\varphi \in [H^2(\Omega)] \mid \varphi = 0 \text{ on } \Gamma_D^\varphi\}, \quad (15e)$$

$$\mathbb{Q}^0 = \{p \in H^1(\Omega) | p = 0 \text{ on } \Gamma_D^p\}. \quad (15f)$$

In (14b), the left superscript n refers to the previous time-step. The history variable \mathbb{H} in (14b) is defined in (13). ■

The history-variable based phase-field hydraulic fracture **Weak form Problem 2** is adopted despite its variational inconsistency, due to its ease of implementation. For variationally consistent formulations, one may pursue the penalty method [66], primal-dual active set method [43,67] or the micromorphic approach [68,69]. In this work, the focus lies on solving the problem with a monolithic solution technique, rather than establishing a variationally consistent phase-field formulation.

2.4. Finite element discretized equations

The Euler–Lagrange (weak form) equations in the **Weak form Problem 2** are discretized using the finite element method [1,3]. Upon introducing interpolation functions, N_i^u , N_i^φ and N_i^p for the displacement, phase-field and the fluid pressure, the corresponding continuous fields (\mathbf{u} , φ , p) are approximated as,

$$\mathbf{u} = \sum_{i=1}^m N_i^u \hat{\mathbf{u}}, \quad \varphi = \sum_{i=1}^m N_i^\varphi \hat{\varphi}, \quad \text{and} \quad p = \sum_{i=1}^n N_i^p \hat{p}, \quad (16)$$

i representing the i th node in a finite element mesh comprising of m nodes. Note the difference in the interpolation functions for the various fields. For the Taylor–Hood elements adopted in this work, m is the total number of nodes (interpolating quadratic approximations for \mathbf{u} and φ), while n represents the number of vertex nodes (interpolating linear approximations for p). Thereafter, the spatial derivatives of the interpolation functions N_i^u , N_i^φ and N_i^p in a two-dimensional case are expressed as,

$$\mathbf{B}_i^u = \begin{bmatrix} N_{i,x}^u & 0 \\ 0 & N_{i,y}^u \\ N_{i,y}^u & N_{i,x}^u \end{bmatrix}, \quad \mathbf{B}_i^\varphi = \begin{bmatrix} N_{i,x}^\varphi \\ N_{i,y}^\varphi \end{bmatrix}, \quad \text{and} \quad \mathbf{B}_i^p = \begin{bmatrix} N_{i,x}^p \\ N_{i,y}^p \end{bmatrix}. \quad (17)$$

Here, the subscripts $,x$ and $,y$ indicate spatial derivatives in x and y directions respectively. Using (17), the strain (ϵ), and the gradients of the phase-field ($\nabla\varphi$) and fluid pressure (∇p) are defined as,

$$\epsilon = \sum_{i=1}^m \mathbf{B}_i^u \hat{\mathbf{u}}_i, \quad \nabla\varphi = \sum_{i=1}^m \mathbf{B}_i^\varphi \hat{\varphi}_i, \quad \text{and} \quad \nabla p = \sum_{i=1}^n \mathbf{B}_i^p \hat{p}_i. \quad (18)$$

Finally, the phase-field hydraulic fracture **Discrete Problem 1** is obtained upon inserting (16)–(18) in the **Weak form Problem 2**. Note that the test functions are also defined similar to (16), following the Bubnov–Galerkin method. The detailed derivation is skipped here for brevity. Interested readers may refer to De Borst et al. [70] for finer details on finite element discretization of Euler–Lagrange equations.

Discrete Problem 1. Compute the solution update vector $\mathbf{s}_{k+1} = \{\Delta\hat{\mathbf{u}}; \Delta\hat{p}; \Delta\hat{\varphi}\}$ for the current iteration $k + 1$ using

$$\underbrace{\begin{bmatrix} \mathbf{K}^{uu} & \mathbf{K}^{up} & \mathbf{K}^{u\varphi} \\ \mathbf{K}^{pu} & \mathbf{K}^{pp} & \mathbf{K}^{p\varphi} \\ \mathbf{K}^{\varphi u} & \mathbf{K}^{\varphi p} & \mathbf{K}^{\varphi\varphi} \end{bmatrix}}_{\text{Stiffness matrix, } \mathbf{K}_k} \underbrace{\begin{Bmatrix} \Delta\hat{\mathbf{u}} \\ \Delta\hat{p} \\ \Delta\hat{\varphi} \end{Bmatrix}}_{\mathbf{s}_{k+1}} = \underbrace{\begin{Bmatrix} \mathbf{0} \\ \mathbf{f}^{\text{ext},p} \\ \mathbf{0} \end{Bmatrix}}_{\text{Residual, } \mathbf{r}_k} - \underbrace{\begin{Bmatrix} \mathbf{f}^{\text{int},u} \\ \mathbf{f}^{\text{int},p} \\ \mathbf{f}^{\text{int},\varphi} \end{Bmatrix}}_{\mathbf{r}_k}, \quad (19a)$$

and update the solution,

$$\begin{Bmatrix} \hat{\mathbf{u}} \\ \hat{p} \\ \hat{\varphi} \end{Bmatrix}_{k+1} = \begin{Bmatrix} \hat{\mathbf{u}} \\ \hat{p} \\ \hat{\varphi} \end{Bmatrix}_k + \begin{Bmatrix} \Delta\hat{\mathbf{u}} \\ \Delta\hat{p} \\ \Delta\hat{\varphi} \end{Bmatrix}_{k+1}, \quad (19b)$$

until the norm of the residual is sufficiently small. The stiffness matrix components are given by,

$$\begin{aligned} \mathbf{K}^{uu} &= \mathcal{A} \int_{\Omega_{el}} [\mathbf{B}^u]^T \underbrace{\left(g(\varphi) \frac{\partial \sigma^+}{\partial \epsilon} + \frac{\partial \sigma^-}{\partial \epsilon} \right)}_{\mathbf{D}} [\mathbf{B}^u] d\Omega, \\ \mathbf{K}^{u\varphi} &= \mathcal{A} \int_{\Omega_{el}} [\mathbf{B}^u]^T (g'(\varphi) \sigma^+) [\mathbf{N}^\varphi] d\Omega, \\ \mathbf{K}^{up} &= \mathcal{A} \int_{\Omega_{el}} [\mathbf{B}^u]^T (-\alpha \mathbf{I}_v) [\mathbf{N}^p] d\Omega, \\ \mathbf{K}^{pu} &= -\frac{1}{\Delta t} [\mathbf{K}^{up}]^T, \\ \mathbf{K}^{pp} &= \mathcal{A} \int_{\Omega_{el}} [\mathbf{B}^p]^T \mathbf{K}_{\text{eff}} [\mathbf{B}^p] \\ &\quad + [\mathbf{N}^p]^T \frac{1}{M} [\mathbf{N}^p] d\Omega, \end{aligned} \quad (19c)$$

$$\begin{aligned}
\mathbf{K}^{p\varphi} &= \mathcal{A} \int_{\Omega_{el}} [\mathbf{B}^p]^T \frac{\partial \mathbf{K}_{\text{eff}}}{\partial \varphi} [\mathbf{N}^\varphi] \\
&\quad + [\mathbf{N}^p]^T \frac{\partial(1/M)}{\partial \varphi} \left(\frac{p-n}{\Delta t} \right) [\mathbf{N}^\varphi] d\Omega, \\
\mathbf{K}^{\varphi u} &= \mathcal{A} \int_{\Omega_{el}} [\mathbf{N}^u]^T \left(g'(\varphi) \frac{\partial \mathbb{H}}{\partial \epsilon} \right) [\mathbf{B}^\varphi] d\Omega, \\
\mathbf{K}^{\varphi p} &= \mathbf{0}, \\
\mathbf{K}^{\varphi\varphi} &= \mathcal{A} \int_{\Omega_{el}} [\mathbf{B}^\varphi]^T \left(\frac{G_c l}{c_w} \right) [\mathbf{B}^\varphi] \\
&\quad + [\mathbf{N}^\varphi]^T \left(\frac{G_c}{c_w l} w''(\varphi) + g''(\varphi) \frac{\partial \mathbb{H}}{\partial \epsilon} \right) [\mathbf{N}^\varphi] d\Omega,
\end{aligned}$$

and the internal force vector components are computed as

$$\begin{aligned}
\mathbf{f}^{\text{ext},p} &= \mathcal{A} \int_{\Gamma_{N,el}} [\mathbf{N}^p]^T q d\Gamma, \\
\mathbf{f}^{\text{int},u} &= \mathcal{A} \int_{\Omega_{el}} [\mathbf{B}^u]^T (g(\varphi) \boldsymbol{\sigma}^+ + \boldsymbol{\sigma}^- - \alpha p \mathbf{I}_v) d\Omega, \\
\mathbf{f}^{\text{int},\varphi} &= \mathcal{A} \int_{\Omega_{el}} [\mathbf{B}^\varphi]^T \frac{G_c l}{c_w} \nabla \varphi \\
&\quad + [\mathbf{N}^\varphi]^T \left(g'(\varphi) \mathbb{H} + \frac{G_c}{c_w l} w'(\varphi) \right) d\Omega, \\
\mathbf{f}^{\text{int},p} &= \mathcal{A} \int_{\Omega_{el}} [\mathbf{B}^p]^T (\mathbf{K}_{\text{eff}} \nabla p) \\
&\quad + [\mathbf{N}^p]^T \left(\frac{1}{M} \frac{p-n}{\Delta t} + \alpha \frac{\epsilon_{\text{vol}} - n}{\Delta t} \right) d\Omega,
\end{aligned} \tag{19d}$$

Note that \mathcal{A} is an assembly operator that maps element contributions to their global counterparts. Furthermore, \mathbf{I}_v is the Voigt representation of the identity matrix, the left superscript n refers to the previous time step, and \mathcal{H} is the Heaviside function. The material stiffness matrix \mathbf{D} depends on the chosen strain energy density split. The history variable \mathbb{H} is defined in (13). ■

The phase-field hydraulic fracture [Discrete Problem 1](#) is non-convex, resulting in poor convergence behaviour of the conventional Newton–Raphson method. In particular, the block $\mathbf{K}^{u\varphi}$ contributes to the divergence of the iterative process at the onset of fracture [43,71]. Recently, the arc-length method augmented with a dissipation-based constraint has been demonstrated as a convergent monolithic solution technique for phase-field fracture models [45,47,48], albeit for linear elastic fracture mechanics problems. In the next section, the limitations in straight-forward extension of the arc-length method to hydraulic fracturing problems is discussed. This is followed by a novel arc-length method construct, suited for hydraulic fracturing problems.

3. A novel arc-length method

The conventional arc-length method [72,73], designed for structural instability problems, introduces a parametrization of the external force (load) \mathbf{f}^{ext} as,

$$\mathbf{f}^{\text{ext}} = \lambda \hat{\mathbf{f}}^{\text{ext}}. \tag{20}$$

Here, λ is scalar load parameter and $\hat{\mathbf{f}}^{\text{ext}}$ is a unit external force. The load parameter λ augments the solution space as an additional unknown. Thereafter, an arc-length constraint equation is incorporated into the system of equations to retain its determinacy. In a discrete ‘matrix–vector’ sense (similar to (19a) in [Discrete Problem 1](#)), the system of equations assume the form,

$$\underbrace{\begin{bmatrix} \mathbf{K}^{UU} & \mathbf{K}^{U\lambda} \\ \mathbf{K}^{\lambda U} & \mathbf{K}^{\lambda\lambda} \end{bmatrix}}_{\text{Stiffness matrix, } \mathbf{K}_k} \underbrace{\begin{Bmatrix} \Delta \tilde{\mathbf{U}} \\ \Delta \tilde{\lambda} \end{Bmatrix}}_{\mathbf{s}_{k+1}} = \underbrace{\begin{Bmatrix} \lambda \hat{\mathbf{f}}^{\text{ext}} \\ 0 \end{Bmatrix}}_{\text{Residual, } \mathbf{r}_k} - \begin{Bmatrix} \mathbf{f}^{\text{int},U} \\ g_{\text{arc}} \end{Bmatrix}. \tag{21}$$

In the context of the phase-field hydraulic fracturing problem, one may assume the solution space $\mathbf{U} := \{\mathbf{u}, p, \varphi\}$. The scalar arc-length constraint equation is designated as g_{arc} . The system of Eqs. (21) has been adopted for phase-field modelling of fractures in linear elastic media [45,47,48]. Therein, the solution space $\mathbf{U} := \{\mathbf{u}, \varphi\}$. Also, these problems are driven by mechanical external forces that vary over the loading process. In contrast, hydraulic fracturing problems in this work are driven by a constant external flux. As such, the notion of the load factor λ is rendered surplus. This motivates the need for an alternative arc-length method construct.

3.1. Time step-size as the scaling parameter

In this work, an arc-length method is proposed, wherein the current time step-size Δt is considered as the scalar unknown corresponding to the arc-length constraint equation g_{arc} . Consequently, the discrete system of equations assume the form,

$$\underbrace{\begin{bmatrix} \mathbf{K}^{UU} & \mathbf{K}^{U\Delta t} \\ \mathbf{K}^{\Delta tU} & \mathbf{K}^{\Delta t\Delta t} \end{bmatrix}}_{\text{Stiffness matrix, } \mathbf{K}_k} \underbrace{\begin{Bmatrix} \Delta \tilde{\mathbf{U}} \\ \Delta \tilde{t} \end{Bmatrix}}_{s_{k+1}} = \underbrace{\begin{Bmatrix} \mathbf{f}^{\text{ext}} \\ 0 \end{Bmatrix}}_{\text{Residual, } \mathbf{r}_k} - \underbrace{\begin{Bmatrix} \mathbf{f}^{\text{int},U} \\ g_{\text{arc}} \end{Bmatrix}}_{\text{}}. \quad (22)$$

Unlike the conventional arc-length method (21), the time step-size computing variant (22) does not parametrize the external load vector \mathbf{f}_{ext} . This allows an arbitrary temporal evolution of \mathbf{f}_{ext} , which, in the case of hydraulic fracturing problems remain constant in time.

3.2. Arc-length constraint

Having established an arc-length method construct for hydraulic fracturing problems, the focus is shifted to an appropriate choice of the arc-length constraint equation. When the arc-length method was conceived as a solution technique meant to capture the snap-back and snap-through instabilities associated with geometrically nonlinear problems [72,73], several arc-length constraint equations were proposed. Some of these equations may be cast into a generic expression as,

$$g_{\text{arc}}(\Delta \mathbf{u}, \Delta \lambda, \Delta s) := \Delta \mathbf{u}^T \Delta \mathbf{u} + \psi \Delta \lambda \hat{\mathbf{f}}_{\text{ext}}^T \hat{\mathbf{f}}_{\text{ext}} - \Delta s = 0, \quad (23)$$

where, $\Delta \mathbf{u}$ represents the displacement increment, Δs is the arc-length, and ψ is user-defined scalar. Based on the choice of ψ , the different arc-length constraint variants are obtained. For instance, choosing $\psi = 0$ yields the cylindrical arc-length constraint equation, while $\psi = 1$ and $\psi > 1$ result in the spherical and elliptic variants, respectively. For a comprehensive review of these variants, the reader is referred to [74,75].

In the context of dissipative materials, Verhoosel et al. [76] reported that the arc-length constraint equation (23) does not perform well. The authors attributed this observation to the localization of the deformation into narrow bands, which renders controlling the solution through a global constraint inadequate. As a solution, the energy release rate-based arc-length constraint was proposed as,

$$g_{\text{arc}}(\Delta \mathbf{u}, \Delta \lambda, \Delta s) := \frac{1}{2} [\hat{\mathbf{f}}_{\text{ext}}]^T (\lambda_n \Delta \mathbf{u} - \Delta \lambda \mathbf{u}_n) - \Delta s = 0, \quad (24)$$

where variables with a subscript n corresponds to the previous converged step. The energy release rate-based constraint equation has been adopted for phase-field fracture models in [46,77], albeit for a limited set of linear elastic fracture problems. Due to its reliance on the scaling of the external force vector, a straight-forward adaption in the phase-field hydraulic fracturing model is not possible.

Recently, Bharali et al. [45] proposed an alternative arc-length constraint equation, based on the incremental phase-field fracture energy $\Delta \Psi_{\text{frac}}$. The constraint equation is given by,

$$g_{\text{arc}}(\varphi, \Delta \varphi, \Delta s) := \underbrace{\int_{\Omega} \frac{G_c}{c_w l} (w'(\varphi) \Delta \varphi + 2l^2 \nabla \varphi \cdot \nabla \Delta \varphi) \, d\Omega}_{\Delta \Psi_{\text{frac}}} - \Delta s = 0. \quad (25)$$

Unlike the energy release rate-based arc-length constraint (24), the incremental phase-field fracture energy based constraint (25) does not depend on the unit external force or its scaling load parameter λ . As such, it is suited to hydraulic fracturing problems. However, the constraint (25) results in a sparse $\mathbf{K}^{\Delta tU}$ block (see (22)). This could lead to a poorly conditioned system of equations or a nearly singular Stiffness matrix [78]. Setting $\mathbf{K}^{\Delta t\Delta t} = \kappa$, where $\kappa > 0$ circumvents these issues, however, at the cost of an inferior convergence rate.

One may construct an alternative, yet equivalent arc-length constraint equation, which results in a comparatively dense $\mathbf{K}^{\Delta tU}$ block. To that end, the phase-field fracture evolution Eq. (14b) is utilized and the test function $\delta \varphi := \Delta \varphi$ is assumed. Thereafter, on substituting $\Delta \Psi_{\text{frac}}$ from (25), the alternative arc-length constraint equation is obtained as,

$$g_{\text{arc}}(\mathbf{u}, \varphi, \Delta \varphi, \Delta s) := \int_{\Omega} (g^n(\varphi) - g(\varphi)) \mathbb{H} \, d\Omega - \Delta s = 0. \quad (26)$$

3.3. Finite element discretized equations

The finite element discretized equations in Discrete Problem 1 is extended with the time step-size computing arc-length method (22) and constraint (26). This results in the Discrete Problem 2.

Discrete Problem 2. Compute the solution update vector $s_{k+1} = \{\Delta \tilde{\mathbf{u}}; \Delta \tilde{p}; \Delta \tilde{\varphi}; \Delta \tilde{t}\}$ for the current iteration $k + 1$ using

$$\underbrace{\begin{bmatrix} \mathbf{K}^{uu} & \mathbf{K}^{up} & \mathbf{K}^{u\varphi} & \mathbf{K}^{u\Delta t} \\ \mathbf{K}^{pu} & \mathbf{K}^{pp} & \mathbf{K}^{p\varphi} & \mathbf{K}^{p\Delta t} \\ \mathbf{K}^{\varphi u} & \mathbf{K}^{\varphi p} & \mathbf{K}^{\varphi\varphi} & \mathbf{K}^{\varphi\Delta t} \\ \mathbf{K}^{\Delta t u} & \mathbf{K}^{\Delta t p} & \mathbf{K}^{\Delta t\varphi} & \mathbf{K}^{\Delta t\Delta t} \end{bmatrix}}_{\text{Stiffness matrix, } \mathbf{K}_k} \underbrace{\begin{Bmatrix} \Delta \tilde{\mathbf{u}} \\ \Delta \tilde{p} \\ \Delta \tilde{\varphi} \\ \Delta \tilde{t} \end{Bmatrix}}_{s_{k+1}} = \underbrace{\begin{Bmatrix} \mathbf{0} \\ \mathbf{f}^{\text{ext},p} \\ \mathbf{0} \\ 0 \end{Bmatrix}}_{\text{Residual, } \mathbf{r}_k} - \underbrace{\begin{Bmatrix} \mathbf{f}^{\text{int},u} \\ \mathbf{f}^{\text{int},p} \\ \mathbf{f}^{\text{int},\varphi} \\ g_{\text{arc}} \end{Bmatrix}}_{\text{Residual, } \mathbf{r}_k}, \quad (27a)$$

and update the solution,

$$\begin{Bmatrix} \tilde{\mathbf{u}} \\ \tilde{p} \\ \tilde{\varphi} \\ \tilde{t} \end{Bmatrix}_{k+1} = \begin{Bmatrix} \tilde{\mathbf{u}} \\ \tilde{p}_w \\ \tilde{\varphi} \\ \tilde{t} \end{Bmatrix}_k + \begin{Bmatrix} \Delta \tilde{\mathbf{u}} \\ \Delta \tilde{p} \\ \Delta \tilde{\varphi} \\ \Delta \tilde{t} \end{Bmatrix}_{k+1}, \quad (27b)$$

until the norm of the residual is sufficiently small. The stiffness matrix components are given by,

$$\begin{aligned} \mathbf{K}^{uu} &= \mathcal{A} \int_{\Omega_{el}} [\mathbf{B}^u]^T \underbrace{\left(g(\varphi) \frac{\partial \sigma^+}{\partial \epsilon} + \frac{\partial \sigma^-}{\partial \epsilon} \right)}_{\mathbf{D}} [\mathbf{B}^u] d\Omega, \\ \mathbf{K}^{u\varphi} &= \mathcal{A} \int_{\Omega_{el}} [\mathbf{B}^u]^T (g'(\varphi) \sigma^+) [\mathbf{N}^\varphi] d\Omega, \\ \mathbf{K}^{up} &= \mathcal{A} \int_{\Omega_{el}} [\mathbf{B}^u]^T (-\alpha \mathbf{I}_v) [\mathbf{N}^p] d\Omega, \\ \mathbf{K}^{u\Delta t} &= \mathbf{0}, \\ \mathbf{K}^{pu} &= -\frac{1}{\Delta t} [\mathbf{K}^{up}]^T, \\ \mathbf{K}^{pp} &= \mathcal{A} \int_{\Omega_{el}} [\mathbf{B}^p]^T \mathbf{K}_{\text{eff}} [\mathbf{B}^p] \\ &\quad + [\mathbf{N}^p]^T \frac{1}{M} [\mathbf{N}^p] d\Omega, \\ \mathbf{K}^{p\varphi} &= \mathcal{A} \int_{\Omega_{el}} [\mathbf{B}^p]^T \frac{\partial \mathbf{K}_{\text{eff}}}{\partial \varphi} [\mathbf{N}^\varphi] \\ &\quad + [\mathbf{N}^p]^T \frac{\partial(1/M)}{\partial \varphi} \left(\frac{p-np}{\Delta t} \right) [\mathbf{N}^\varphi] d\Omega, \\ \mathbf{K}^{p\Delta t} &= -\mathcal{A} \int_{\Omega_{el}} [\mathbf{N}^p]^T \frac{1}{M} \left(\frac{p-np}{\Delta t^2} \right) \\ &\quad - [\mathbf{N}^p]^T \alpha \left(\frac{\epsilon_{\text{vol}} - n \epsilon_{\text{vol}}}{\Delta t^2} \right) d\Omega, \\ \mathbf{K}^{\varphi u} &= \mathcal{A} \int_{\Omega_{el}} [\mathbf{N}^u]^T \left(g'(\varphi) \frac{\partial \mathbb{H}}{\partial \epsilon} \right) [\mathbf{B}^\varphi] d\Omega, \\ \mathbf{K}^{\varphi p} &= \mathbf{0}, \\ \mathbf{K}^{\varphi\varphi} &= \mathcal{A} \int_{\Omega_{el}} [\mathbf{B}^\varphi]^T \left(\frac{G_c l}{c_w} \right) [\mathbf{B}^\varphi] \\ &\quad + [\mathbf{N}^\varphi]^T \left(\frac{G_c}{c_w l} w''(\varphi) + g''(\varphi) \frac{\partial \mathbb{H}}{\partial \epsilon} \right) [\mathbf{N}^\varphi] d\Omega, \\ \mathbf{K}^{\varphi\Delta t} &= \mathbf{0}, \\ \mathbf{K}^{\Delta t u} &= \mathcal{A} \int_{\Omega_{el}} \Delta g(\varphi) \sigma^+ [\mathbf{B}^u] d\Omega, \\ \mathbf{K}^{\Delta t\varphi} &= \mathcal{A} \int_{\Omega_{el}} [\mathbf{N}^\varphi]^T g'(\varphi) \Psi^+ d\Omega, \\ \mathbf{K}^{\Delta t p} &= \mathbf{K}^{\Delta t\Delta t} = \mathbf{0}, \end{aligned} \quad (27c)$$

and the internal force vector components are computed as

$$\mathbf{f}^{\text{ext},p} = \mathcal{A} \int_{\Gamma_{N,el}} [\mathbf{N}^p]^T q d\Gamma,$$

$$\begin{aligned}
\mathbf{f}^{\text{int},u} &= \mathcal{A} \int_{\Omega_{el}} [\mathbf{B}^u]^T (g(\varphi)\boldsymbol{\sigma}^+ + \boldsymbol{\sigma}^- - \alpha p \mathbf{I}_v) d\Omega, \\
\mathbf{f}^{\text{int},\varphi} &= \mathcal{A} \int_{\Omega_{el}} [\mathbf{B}^\varphi]^T \frac{G_c l}{c_w} \nabla \varphi \\
&\quad + [\mathbf{N}^\varphi]^T \left(g'(\varphi) \mathbb{H} + \frac{G_c}{c_w l} w'(\varphi) \right) d\Omega, \\
\mathbf{f}^{\text{int},p} &= \mathcal{A} \int_{\Omega_{el}} [\mathbf{B}^p]^T (\mathbf{K}_{\text{eff}} \nabla p) \\
&\quad + [\mathbf{N}^p]^T \left(\frac{1}{M} \frac{p - {}^n p}{\Delta t} + \alpha \frac{\epsilon_{\text{vol}} - {}^n \epsilon_{\text{vol}}}{\Delta t} \right) d\Omega, \\
g_{\text{arc}} &= \mathcal{A} \int_{\Omega_{el}} \left(\Delta g(\varphi) \Psi^+ \right) d\Omega + \Delta s. \quad \blacksquare
\end{aligned} \tag{27d}$$

3.4. Implementation caveats

The arc-length method does entail some implementation caveats. They are discussed in this section.

Singular Hessian

The stiffness matrix \mathbf{K} in [Discrete Problem 2](#) would be singular if adequate constraints are not enforced, and also at the start of the analysis when the solution is zero. In this work, adequate constraints are always enforced on all problems. The second source of singular stiffness matrix is circumvented by commencing the simulation with the conventional Newton–Raphson method (see [Discrete Problem 1](#)). Thereafter, the switch to the arc-length method may be carried out when the Newton–Raphson method fails to converge or based on some user-defined criterion.

User criterion for switching to the arc-length method

A user-defined criterion for switching from the Newton–Raphson method to the arc-length method may be formulated based on the energy dissipated in a step $\Delta \Psi_{\text{frac}}$. Once it exceeds a certain threshold value, say threshold $\Psi_{\text{frac,th}}$, the switch is carried out. The threshold energy may be either prescribed based on user-intuition or computed using a threshold phase-field φ_{th} as,

$$\Psi_{\text{frac,th}} = \frac{G_c}{c_w l} w(\varphi_{\text{th}}) V_{\text{elem}}, \tag{28}$$

with V_{elem} being the volume of the smallest element in the finite element mesh.

In this work, the switch from the Newton–Raphson method to the arc-length method is made when $\Delta \Psi_{\text{frac}} > \Psi_{\text{frac,th}} = 10^{-7}$ and also when the Newton–Raphson method requires more than 6 iterations to converge in a step.

Adaptive modification of the arc-length

Another key aspect pertaining to the arc-length method is the initial value of the arc-length Δs and its adaptive modifications over the course of the simulation. In this work, the initial value of the arc-length Δs is set to fracture energy dissipated in the previous step, computed using Newton–Raphson method. Although, this value may be conservatively small, it allows a smooth transition from the Newton–Raphson method to the arc-length method.

Furthermore, during the course of simulation, the arc-length Δs is modified adaptively, based on iterations required to achieve convergence `iiter`. Following [Verhoosel et al. \[76\]](#), the arc-length Δs for the current step is computed as,

$$\Delta s = \begin{cases} 1.15 \Delta s_n & \text{if } \text{iiter} < \text{optIter} \\ \Delta s_n 0.5^{0.25(\text{iiter} - \text{optIter})} & \text{otherwise.} \end{cases} \tag{29}$$

where, the subscript n indicates the previous converged step, `optIter` is a user-defined optimum number of iterations.

4. Numerical study

In this section, numerical experiments are carried out on three hydraulic fracturing problems, using the proposed time step-size computing arc-length method. The corresponding geometries have been adopted from Mikelić, Wheeler, and Wick [[26,27](#)], and are presented in [Fig. 1](#). For all problems, the computational domain is a square (4×4 [m²]), embedded with varying initial fracture(s) to demonstrate the complexity of fracture topologies. The Single Natural Fracture (SNF) specimen contains an initial fracture, 0.4 [m] in length and is located midway along the height. Upon injecting fluid into the fracture, a horizontal fracture propagation is expected. The Double Natural Fracture (DNF) specimen adds a vertical initial fracture of length 0.4 [m], at an x-offset 0.6 [m] from the centre of the specimen. A fracture merging event is expected upon injection of fluid into the existing fractures. Finally, the Triple Natural Fracture (TNF) adds an inclined fracture to the DNF specimen. The newly introduced fracture is a line segment from coordinates $(-0.8, -0.3)$ to $(-0.3, -0.8)$ assuming the axes origin placed at the centre of the specimen. The injection of fluid into the existing fractures would result in two fracture merging events. For all problems, the model parameters are presented in

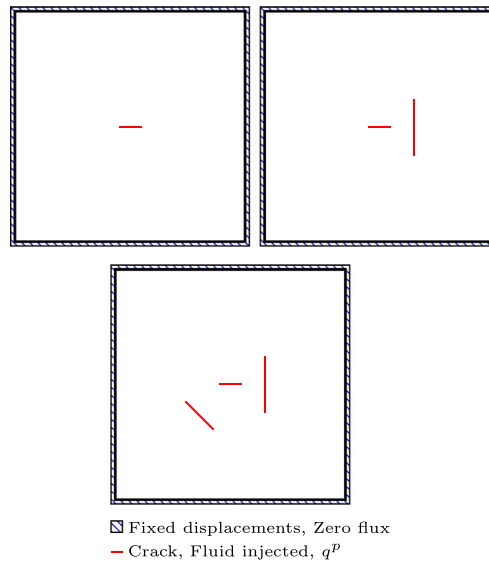


Fig. 1. Specimens with varying initial fractures.

Table 1
Model parameters.

Parameters	Value [Units]
Fracture model	AT2
Energy split	Spectral
E_0	1 [GPa]
ν	0.2 [-]
G_c	1 [N/m]
l	5e-2 [m]
Element size	1/4 [m]
α	1.0 [-]
n	0.4 [-]
$k_{i,b}$	1e-12 [m ²]
μ_f	1e-3 [Pas]
K_s	10 [GPa]
K_f	2 [GPa]
q^p	1e-2 [m/s]
optIter	10 [-]

Table 1. Due to the difference in the formulation of the fluid transport equation in this work compared to Mikelić, Wheeler, and Wick [26,27], additional parameters (K_b , K_f , n) have been utilized.

The specimens in Fig. 1 are discretized with 8-noded Taylor and Hood quadrilateral elements [57], in accordance with the test and trial spaces established in the Weak form Problem 2. Furthermore, a residual-based convergence criterion is adopted for both, the Newton–Raphson method as well as the arc-length method. Convergence is assumed to be achieved when the ratio of the norm of the current residual to residual at the first iteration is less than a certain tolerance, 10^{-4} . Finally, the linear problem within each iteration is solved using the shared-memory Pardiso direct solver from Intel’s oneAPI Math Kernel Library [79].

Fracture topologies and pressure distributions

The phase-field fracture distribution in the SNF specimen is presented in Fig. 2 for different times ($t = 0.001, 0.0365$ and 0.15 [s]) during the analysis. The initial fracture propagates in mode I, a consequence of choosing the spectral decomposition [65] of the strain energy density. The observed fracture pattern is similar to that reported by Mikelić et al. [26], however, with a different timeline. This difference is attributed to the chosen model parameters which differ from Mikelić et al. [26]. Furthermore, adopting the analytical expression for the fracture length as a function of injection time from Detournay [80], the fracture propagation timeline is verified in Appendix.

The development of fluid pressure within the SNF specimen is presented in Fig. 3, for the aforementioned times ($t = 0.001, 0.0365$ and 0.15 [s]) during the analysis. The fluid pressure localizes with higher values observed in the fracture zone ($\varphi > 0$), compared to the bulk (intact) material zone. This localization of the pressure is consequence of enhanced permeability (7) and porosity (9) in the fractures. Fig. 3(b) also presents the development of negative fluid pressures at the fracture tips. Secchi and Schrefler [5] describes

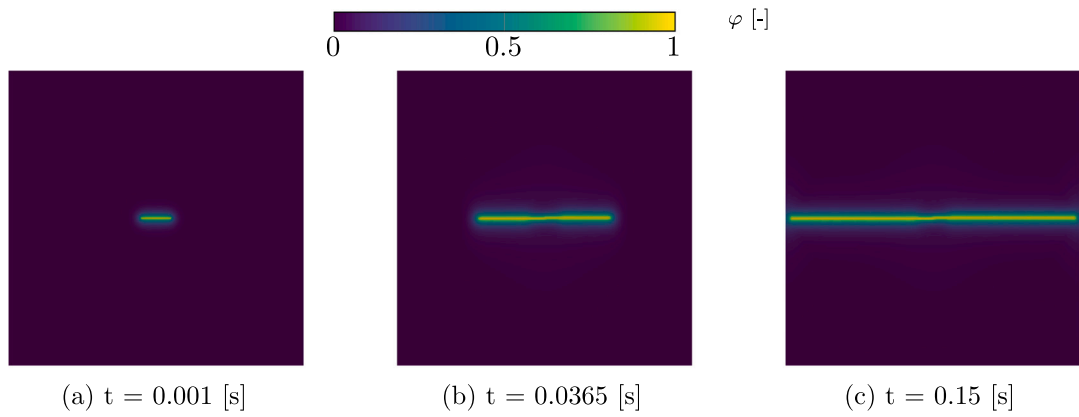


Fig. 2. Figures (a–c) present the distribution of the phase-field variable at the different times during the analysis of the Single Natural Fracture (SNF) specimen.

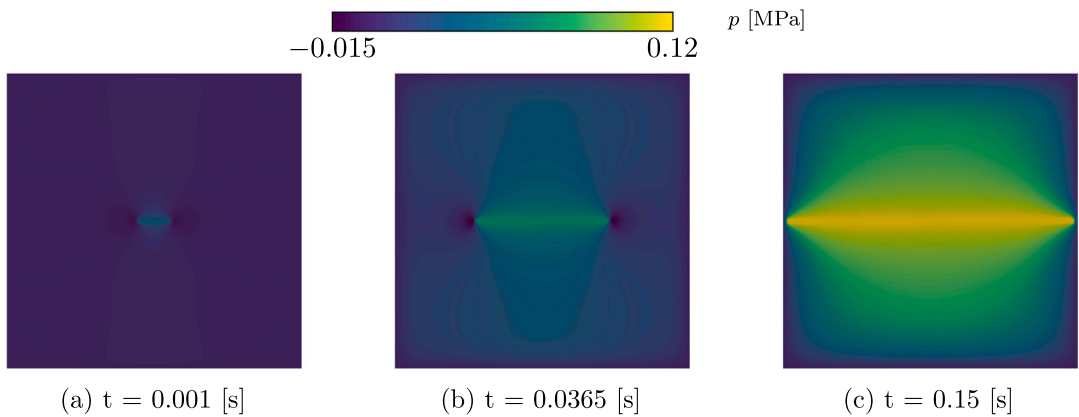


Fig. 3. Figures (a–c) present the distribution of the water pressure at the different times during the analysis of the Single Natural Fracture (SNF) specimen.

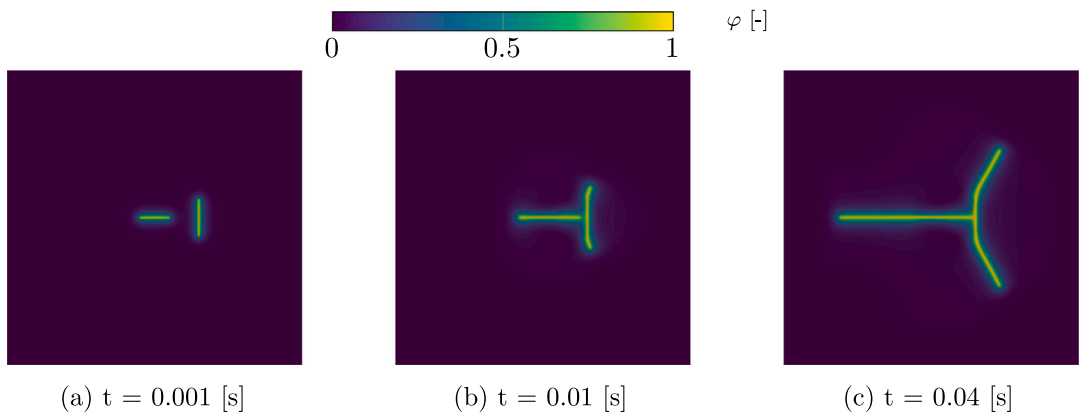


Fig. 4. Figures (a–c) present the distribution of the phase-field variable at the different times during the analysis of the Double Natural Fracture (DNF) specimen.

this phenomenon as ‘fluid lag’, which arises due to a high fracture propagation velocity for a given permeability. In such a scenario, the fluid is not able to flow quickly enough to occupy the fracture space. The reader is referred to [Detournay and Garagash \[81\]](#) for more details.

Fig. 4 presents the phase-field fracture topology observed at different times ($t = 0.001, 0.01$ and 0.04 [s]) during the hydraulic fracturing analysis of the DNF specimen. The final fracture pattern is similar to that reported by [Mikelić, Wheeler, and Wick \[26\]](#) and not the propagation phase. This difference is due to the fluid injection of both fractures in this work, unlike that in [\[26\]](#). Similar

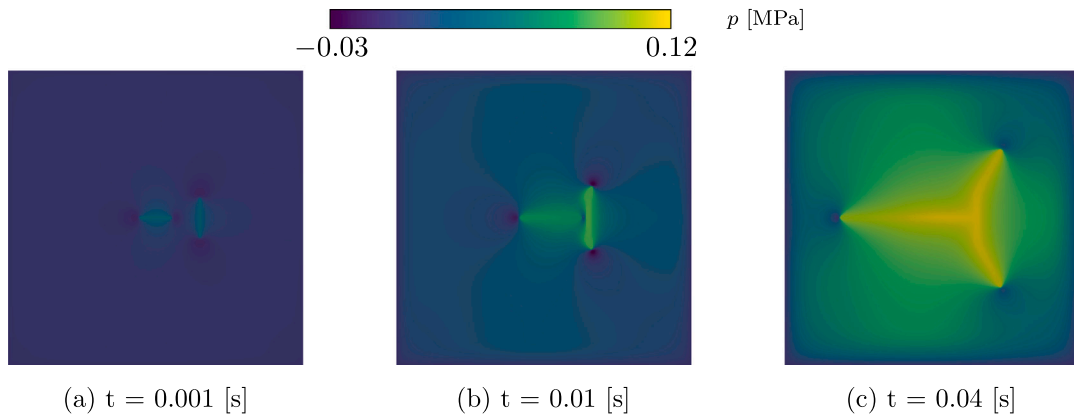


Fig. 5. Figures (a–c) present the distribution of the water pressure at the different times during the analysis of the Double Natural Fracture (DNF) specimen.

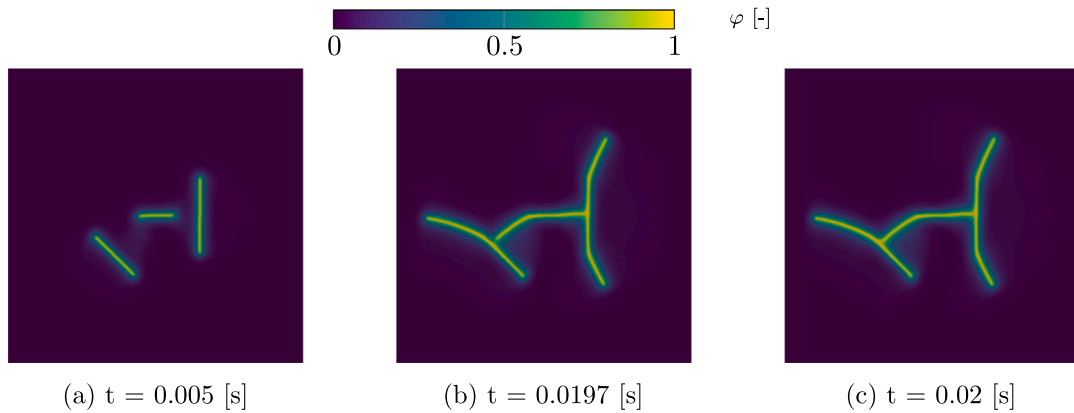


Fig. 6. Figures (a–c) present the distribution of the phase-field variable at the different times during the analysis of the Triple Natural Fracture (TNF) specimen.

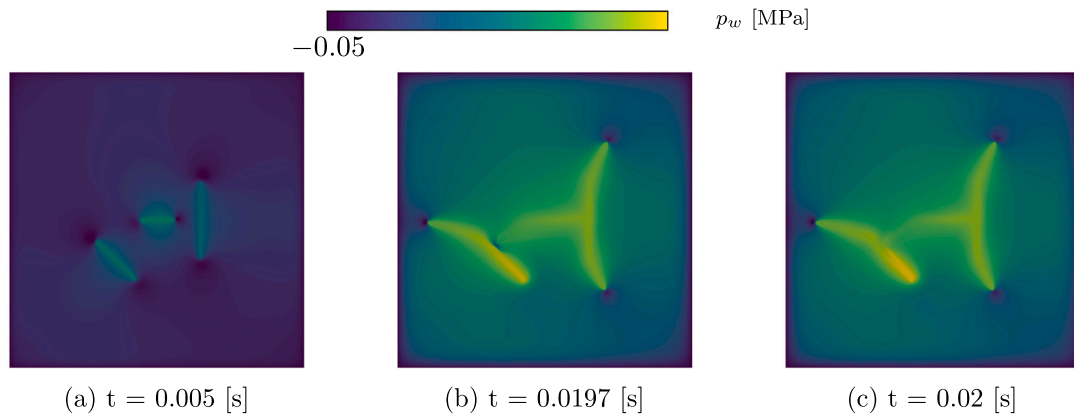


Fig. 7. Figures (a–c) present the distribution of the water pressure at the different times during the analysis of the Triple Natural Fracture (TNF) specimen.

to the SNF specimen, the fracture propagation occurs primarily in mode I due to the spectral decomposition [65] of the strain energy density. However, DNF specimen exhibits a comparatively complex fracture merging behaviour. The arc-length method is able to capture this unstable fracture growth. Furthermore, the water pressure distribution is presented in Fig. 5. Similar to the SNF specimen, the fluid lag phenomenon at the fracture tips as well as the localization of water pressure are observed.

Fig. 6 presents the phase-field fracture distribution at different times ($t = 0.005, 0.0197$ and 0.02 [s]) during the fluid driven fracturing of the TNF specimen. Here, two fracture merging events are observed. From an energy minimization perspective, these events could be seen as competing mechanisms. The first fracture merging event occurs when the initial horizontal fracture propagates and merges with the vertical fracture at $t \approx 0.011$ [s]. Thereafter, at $t \approx 0.0197$ [s] (see Fig. 6(b)), the second

Table 2

Table presents the total numbers of steps and iterations, average iterations and wall time (in seconds) for the SNF, DNF, TNF specimens simulated using the arc-length method with varying iteration terminating tolerances. DOFs is an abbreviation for Degrees of Freedom. Failed indicates the number of steps that did not converge.

Specimen (DOFs)	tol	Steps (Failed)	Total Iters.	Avg. Iters.	Wall time [s]
SNF (274 940)	10^{-4}	320 (25)	2340	7.31	1.750e+04
	10^{-6}	313 (10)	3463	11.06	2.672e+04
	10^{-8}	381 (37)	4584	12.03	6.158e+04
DNF (1 233 924)	10^{-4}	224 (6)	1745	7.79	5.410e+04
	10^{-6}	218 (6)	2216	10.16	7.211e+04
	10^{-8}	192 (14)	2739	14.26	1.059e+05
TNF (1 235 724)	10^{-4}	147 (3)	1144	7.78	3.494e+04
	10^{-6}	191 (9)	1827	9.56	5.952e+04
	10^{-8}	188 (18)	2307	12.27	9.514e+04

fracture merging event occurs. Furthermore, the fluid pressure distribution is presented in Fig. 7, again demonstrating the fluid lag phenomenon.

Performance assessment

This section presents a study on the computational efficiency and robustness of the proposed time step-size computing arc-length method. To that end, the hydraulic fracture simulations are carried out on the SNF, DNF, and TNF specimens with varying iteration terminating tolerances 10^{-4} , 10^{-6} and 10^{-8} . All model parameters remain unchanged from Table 1, albeit the optimal iteration count (`optIter`). Adopting the rationale that a stricter tolerance would entail more iterations to achieve convergence, `optIter` is varied as 10, 14 and 18 corresponding to the tolerances 10^{-4} , 10^{-6} and 10^{-8} , respectively. Thereafter, the total as well as the average number of iterations required for convergence through the simulation are considered as computational efficiency measures, along with the wall time. The simulations are performed on the Chalmers' Centre for Computational Science and Engineering Vera cluster on Intel Xeon Gold 6130.

In the context of problem size, the SNF specimen is discretized with 8-noded quadrilateral Taylor–Hood elements. Adopting the pre-refinement strategy along the expected horizontal fracture propagation zone yields 23 210 elements and 274 940 Degrees of Freedom (DOFs). For the DNF and TNF, the mesh is uniformly refined. The discretized DNF specimen consists of 103 752 elements and 1 233 924 DOFs, while the TNF specimen results in 103 999 elements and 1 235 724 DOFs. Due to the lower number of elements and DOFs, five cores utilized for simulating the SNF specimen, while ten cores are adopted for the DNF and TNF specimen. Furthermore, shared-memory parallelism is adopted for the assembly of the pertinent matrices and vectors. The linear problem in every iteration is solved using the shared memory Pardiso solver from Intel's oneAPI Math Kernel Library [79]. Therein, re-ordering of the matrix is carried out using nested dissection method, and scaling and weighted matching operations are enabled.

Table 2 presents the efficiency measures for the SNF, DNF and TNF specimen. Convergence is achieved for all combinations of specimens and iteration terminating tolerances, thereby demonstrating the robustness of the arc-length method. Due to the implicitly embedded adaptive nature of the arc-length method, the total number of steps required to achieve the final simulation time varies with the chosen tolerance, and varies from specimen to specimen. However, there is no specific trend w.r.t the tolerance. This is due to the implicit adaptivity in the arc-length method, where the current value of the arc-length depends on its previous value and the iterations required to achieve converge in the previous step. One may influence the arc-length update using the parameter `optIter` in (29). The chosen arc-length update may in certain steps, result in a non-convergent iterative process. In that case, the corresponding step is then repeated with an arc-length parameter reduced by 55%. For each problem and chosen tolerance the Failed steps are also presented. Furthermore, as with most well-behaved nonlinear problems, on adopting a stricter tolerance, more iterations are required to achieve converge. Consequently, the simulation wall time also increases.

Next, the computational efficiency of the proposed arc-length method is assessed. To that end, the hydraulic fracturing simulations on the SNF, DNF and TNF specimens are carried out using the BFGS method and the staggered (alternate minimization) solution technique. The iteration terminating tolerance is set to 10^{-4} . Fixed time-step sizes $5 \cdot 10^{-4}$ [s], $2 \cdot 10^{-4}$ [s], and $1 \cdot 10^{-4}$ [s] are adopted for the SNF, DNF, and TNF specimens, respectively. This variation in the time-step sizes results in similar number of steps for BFGS method and the staggered solution technique, as that of the arc-length method for the entire simulation.

Table 3 presents the efficiency measures for the different solution techniques, all with an iteration terminating tolerance of 10^{-4} . The arc-length method utilizes the least number of iterations to converge for all specimens. This also reflects in the simulation wall time. In contrast, the BFGS method requires higher number of iterations to converge. As such, it clocks approximately 9 to 15.5 times the wall time observed with the arc-length method. Furthermore, the staggered solution technique requires the highest number of iterations to achieve convergence. This feature is attributed to the splitting of a fully coupled problem into two sub-problems. Despite the higher number of iterations compared to the BFGS method, the staggered solution technique clocks lower wall times. The reason for this observation lies in the cheaper nature of the linear solves for the individual sub-problems. However, compared to the arc-length method, the staggered solution technique still increases the wall time by a factor of about 5 to 12. Thus, the savings made through cheaper linear solvers is overly compensated by large number of iterations required to achieved convergence.

Additionally, on comparing the data from Tables 3 and 2, one may observe that the arc-length method with stricter iteration terminating tolerances 10^{-6} and 10^{-8} records similar or lower wall time, compared to the BFGS and staggered solution techniques with tolerance 10^{-4} . This further demonstrates the computational efficiency of the arc-length method.

Table 3

Table presents the total numbers of steps and iterations, average iterations and wall time (in seconds) for the SNF, DNF, TNF specimens simulated using the arc-length, BFGS and Staggered methods with iteration terminating tolerance 10^{-4} . DOFs is an abbreviation for Degrees of Freedom. Failed indicates the number of steps that did not achieve convergence. Wall time ratio is a ratio between the wall time recorded by a method to that of the arc-length method.

Specimen (DOFs)	Method	Steps (Failed)	Total Iters.	Avg. Iters.	Wall time [s]	Wall time ratio [-]
SNF (274 940)	Arc-length	320 (25)	2340	7.31	1.750e+04	1
	BFGS	299 (0)	5759	19.26	1.568e+05	8.96
	Staggered	299 (0)	7136	23.87	9.099e+04	5.20
DNF (1 233 924)	Arc-length	214 (2)	1649	7.70	4.861e+04	1
	BFGS	200 (0)	5310	26.55	5.648e+05	11.61
	Staggered	200 (0)	6053	30.26	3.497e+05	7.19
TNF (1 235 724)	Arc-length	147 (3)	1144	7.78	3.494e+04	1
	BFGS	200 (0)	4988	24.94	5.411e+05	15.48
	Staggered	200 (0)	6534	32.67	4.151e+05	11.88

Evolution of time-step size

This section investigates the evolution of the time-step size Δt obtained using the arc-length method (see [Discrete Problem 2](#)). Unlike the conventional incremental iterative methods (e.g., Newton–Raphson, BFGS, Staggered), the arc-length method in this work considers Δt as a scalar unknown, dual to the arc-length constraint equation (26). For this reason, it is imperative to demonstrate physically admissible positive Δt for each step of the simulation. A negative Δt would indicate moving backwards in time, which is not admissible. [Figs. 8\(a\)–8\(c\)](#) present the evolution of Δt (in solid black lines) for the SNF, DNF, and TNF specimens obtained using the arc-length method. A positive Δt is observed at each step, thereby indicating a physically admissible time-dependent hydraulic fracturing processes. One may also observe the Δt in the denominator of the water transport Eq. (14c), which has an asymptote at $\Delta t = 0$. This prevents a negative Δt as long as the starting guess remains positive.

Additionally, for all specimens, the evolution of the time-step size Δt is oscillatory. The reason for this behaviour lies in the adaptive nature of the arc-length Δs , computed based on the iterations required to converge in the previous step (see Eq. (29)). During the fracture merging events (indicated by red dashed lines) in the DNF and TNF specimens, distinct troughs are observed in the Δt curves. During these steps, the arc-length Δs is reduced, which indicates a lower yet finite energy dissipation. Consequently, a lower Δt is obtained as a solution. For these rather complex fracturing steps, the arc-length method converges with less than 17 iterations, while the BFGS and staggered solution techniques require more than 75 and 100, respectively. Beyond these fracture merging events, the evolution of the Δt follows a rising trend (see [Fig. 8](#)).

5. Conclusions and outlook

A novel arc-length method is proposed for simulating hydraulic fracturing in porous media using the phase-field fracture model. The need for a novel solution technique stems from the non-convex nature of the phase-field fracture model, which renders a poor convergence behaviour of conventional solution techniques. The Newton–Raphson method fails to converge during fracture propagation, while the BFGS method and the staggered solution technique demonstrate slow convergence.

Unlike conventional arc-length methods, the arc-length method in this work considers the time-step size as the scalar unknown. Consequently, the external load (in this context, the fluid flux) becomes independent and user-defined. Theoretically, one may prescribe an arbitrary time-dependent fluid flux. However, in this work and in previous phase-field hydraulic fracturing simulations, the fluid flux is kept constant. Correspondingly, a dissipation-based arc-length constraint is adopted to maintain the determinacy of the system of equations.

The robustness of the arc-length method is demonstrated on hydraulic fracturing problems of increasing complexity in terms of fracture topology. Three specimens with one, two and three initial fractures are considered, where the fluid is injected. While the specimen with one fracture results in extension of the initial crack, the latter two specimens with multiple initial fractures demonstrate fracture merging phenomenon. The arc-length method is able to perform these hydraulic fracturing simulations for a range of lenient to strict iteration terminating tolerances (10^{-4} , 10^{-6} and 10^{-8}).

Furthermore, a performance comparison of the arc-length method versus the BFGS method and the staggered method is carried out. These latter methods are popular in the phase-field fracture literature and widely adopted solution techniques. The arc-length method outperforms both aforementioned methods in terms of number of iterations required to converge, and consequently the simulation wall time. For the specimens adopted in this work, the arc-length method records computation times that are about 9 to 15.5 times lower wall time compared to the BFGS method, and approximately 5 to 12 times lower than the staggered solution technique. Here, the lower bound corresponds to the simple case of the specimen with a single initial fracture while the relative advantage of the proposed method increases for more complex cases that involve crack merging.

Finally, the robustness and computational efficiency of the arc-length method over the state-of-the-art BFGS method and staggered solution techniques opens new possibilities. In this context, a straight-forward extension can be made towards similar transport mechanism driven fracturing phenomenon. Such examples include corrosion, thermal flux, and hygroscopic damage/fracturing.

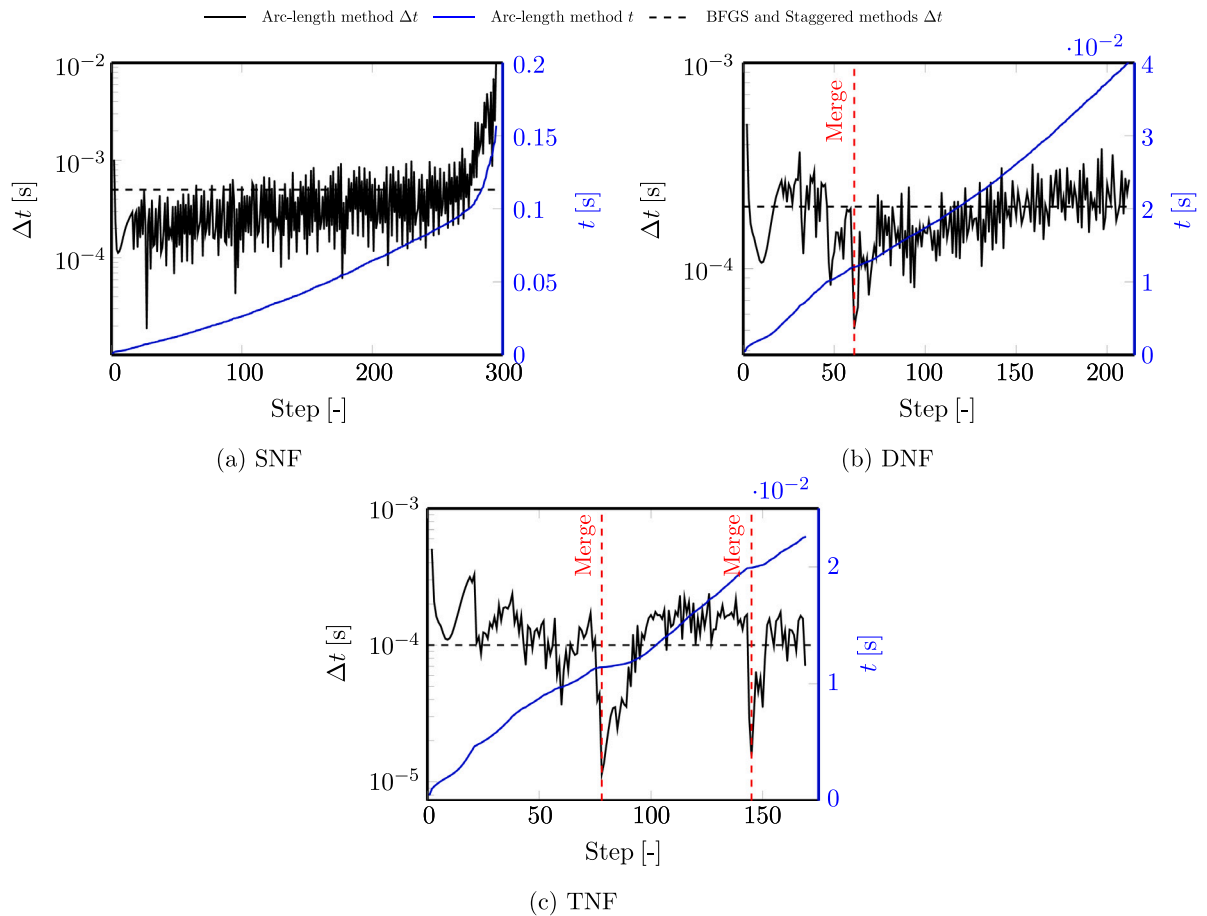


Fig. 8. Figures present the non-linear evolution of the time-step size Δt and the time t (solid black and blue lines, respectively) obtained using the arc-length method for the SNF, DNF and TNF specimen. The black dashed lines show the fixed Δt for the BFGS and staggered solution techniques. The red dashed lines indicate fracture merging events (see Figs. 4 and 6). (For interpretation of the references to colour in this figure legend, the reader is referred to the web version of this article.)

6. Software implementation and data availability

The phase-field hydraulic fracturing model and the solution techniques (arc-length, BFGS and staggered solvers) used in this work are part of the open-source software `falcon`. The software is available on Github (<https://github.com/ritukeshbharali/falcon>), and is distributed under the GNU LGPL 2.1 license.

CRedit authorship contribution statement

Ritukesh Bharali: Writing – review & editing, Writing – original draft, Validation, Software, Methodology, Investigation, Conceptualization. **Frans P. van der Meer:** Writing – review & editing, Writing – original draft, Validation, Supervision, Software, Methodology, Investigation, Conceptualization. **Fredrik Larsson:** Writing – review & editing, Writing – original draft, Visualization, Validation, Supervision, Project administration, Methodology, Investigation, Funding acquisition, Conceptualization. **Ralf Jänicke:** Writing – review & editing, Writing – original draft, Visualization, Validation, Supervision, Project administration, Methodology, Investigation, Funding acquisition, Conceptualization.

Declaration of competing interest

The authors declare that they have no known competing financial interests or personal relationships that could have appeared to influence the work reported in this paper.

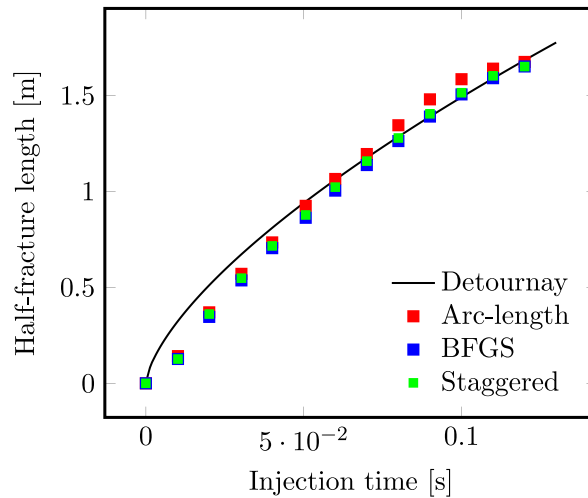


Fig. A.1. Comparison of fracture length obtaining with different methods w.r.t Detournay's analytical solution [80] for the SNF specimen.

Acknowledgements

The financial support from the Swedish Research Council for Sustainable Development (FORMAS), Sweden under Grant 2018-01249 and the Swedish Research Council (VR), Sweden under Grant 2017-05192 is gratefully acknowledged. The first author would like to thank the Faculty of Civil Engineering and Geosciences, TU Delft for facilitating the research visit, and Dr. Erik Jan Lingen at Dynaflo Research Group for support with the Jem and Jive libraries.

Appendix. Comparison of Detournay's analytical solution for fracture length with numerically obtained solutions

The propagation of hydraulic fracture in an impermeable elastic medium has been studied by Detournay [80] adopting a problem similar to the Single Natural Fracture (SNF) specimen in Fig. 1. Assuming symmetry and a toughness dominated regime (due to the creation of new fracture surfaces), an analytical expression for the half-fracture length has been proposed as,

$$l_{\text{fracture}} = \frac{2}{\pi^{2/3}} \left(\frac{E'qt}{K'} \right), \quad (\text{A.1})$$

where, q is the injection rate assuming symmetry, t is the injection time, and parameters E' and K' are computed as,

$$E' = \frac{E_0}{1-\nu^2} \quad \text{and} \quad K' = 4 \left(\frac{2}{\pi} \right)^{1/2} \sqrt{\frac{G_c E_0}{1-\nu^2}}. \quad (\text{A.2})$$

Here, E_0 , ν and G_c represent the Young's modulus, Poisson's ratio, and the Griffith fracture toughness.

Adapting (A.1) in the context for the SNF specimen with model parameters specified in Table 1, the analytical solution for the half-fracture length versus the injection time is presented in Fig. A.1. Therein, the discrete points refer to the half-fracture lengths obtained numerically using the different solution techniques (arc-length, BFGS and staggered solvers). Due to the smeared nature of the phase-field fracture model, the fracture lengths are measured using a threshold phase-field value of 0.8. Depending on the chosen length-scale and threshold value, the fracture lengths may differ, albeit minimally. Finally, the similarity of the fracture lengths reported by different methods and their proximity to the analytical solution presents a reasonable verification of the modelled fracture propagation process.

Data availability

Section 6 of this article addresses the code and data availability.

References

- [1] O.C. Zienkiewicz, R.L. Taylor, P. Nithiarasu, J. Zhu, *The Finite Element Method*, vol. 3, McGraw-hill London, 1977.
- [2] T.J. Hughes, *The Finite Element Method: Linear Static and Dynamic Finite Element Analysis*, Dover Publications, New York, ISBN: 978-0-486-41181-1, 2012.
- [3] S.C. Brenner, L.R. Scott, L.R. Scott, *The Mathematical Theory of Finite Element Methods*, vol. 3, Springer, ISBN: 978-0-387-75934-0, 2008, <http://dx.doi.org/10.1007/978-0-387-75934-0>.

- [4] S. Secchi, L. Simoni, B.A. Schrefler, Mesh adaptation and transfer schemes for discrete fracture propagation in porous materials, *Int. J. Numer. Anal. Methods Geomech.* 31 (2) (2007) 331–345, <http://dx.doi.org/10.1002/nag.581>.
- [5] S. Secchi, B.A. Schrefler, A method for 3-D hydraulic fracturing simulation, *Int. J. Fract.* (ISSN: 1573-2673) 178 (1) (2012) 245–258, <http://dx.doi.org/10.1007/s10704-012-9742-y>.
- [6] N. Sukumar, N. Moës, B. Moran, T. Belytschko, Extended finite element method for three-dimensional crack modelling, *Int. J. Numer. Methods Eng.* 48 (11) (2000) 1549–1570, [http://dx.doi.org/10.1002/1097-0207\(20000820\)48:11<1549::AID-NME955>3.0.CO;2-A](http://dx.doi.org/10.1002/1097-0207(20000820)48:11<1549::AID-NME955>3.0.CO;2-A).
- [7] N. Moës, T. Belytschko, Extended finite element method for cohesive crack growth, *Eng. Fract. Mech.* 69 (7) (2002) 813–833, [http://dx.doi.org/10.1016/S0013-7944\(01\)00128-X](http://dx.doi.org/10.1016/S0013-7944(01)00128-X).
- [8] E. Gordeliy, A. Peirce, Coupling schemes for modeling hydraulic fracture propagation using the XFEM, *Comput. Methods Appl. Mech. Engrg.* 253 (2013) 305–322, <http://dx.doi.org/10.1016/j.cma.2012.08.017>.
- [9] E. Gordeliy, A. Peirce, Implicit level set schemes for modeling hydraulic fractures using the XFEM, *Comput. Methods Appl. Mech. Engrg.* 266 (2013) 125–143, <http://dx.doi.org/10.1016/j.cma.2013.07.016>.
- [10] E. Gordeliy, A. Peirce, Enrichment strategies and convergence properties of the XFEM for hydraulic fracture problems, *Comput. Methods Appl. Mech. Engrg.* (ISSN: 0045-7825) 283 (2015) 474–502, <http://dx.doi.org/10.1016/j.cma.2014.09.004>.
- [11] P. Gupta, C.A. Duarte, Coupled hydromechanical-fracture simulations of nonplanar three-dimensional hydraulic fracture propagation, *Int. J. Numer. Anal. Methods Geomech.* 42 (1) (2018) 143–180, <http://dx.doi.org/10.1002/nag.2719>.
- [12] M. Sheng, G. Li, D. Sutula, S. Tian, S.P. Bordas, XFEM modeling of multistage hydraulic fracturing in anisotropic shale formations, *J. Pet. Sci. Eng.* (ISSN: 0920-4105) 162 (2018) 801–812, <http://dx.doi.org/10.1016/j.petrol.2017.11.007>.
- [13] A. Khoei, M. Vahab, M. Hirmand, An enriched-FEM technique for numerical simulation of interacting discontinuities in naturally fractured porous media, *Comput. Methods Appl. Mech. Engrg.* (ISSN: 0045-7825) 331 (2018) 197–231, <http://dx.doi.org/10.1016/j.cma.2017.11.016>.
- [14] A. Jafari, M. Vahab, N. Khalili, Fully coupled XFEM formulation for hydraulic fracturing simulation based on a generalized fluid leak-off model, *Comput. Methods Appl. Mech. Engrg.* (ISSN: 0045-7825) 373 (2021) 113447, <http://dx.doi.org/10.1016/j.cma.2020.113447>.
- [15] D. Dugdale, Yielding of steel sheets containing slits, *J. Mech. Phys. Solids* (ISSN: 0022-5096) 8 (2) (1960) 100–104, [http://dx.doi.org/10.1016/0022-5096\(60\)90013-2](http://dx.doi.org/10.1016/0022-5096(60)90013-2).
- [16] G. Barenblatt, in: H. Dryden, T. von Kármán, G. Kuerti, F. van den Dungen, L. Howarth (Eds.), *The Mathematical Theory of Equilibrium Cracks in Brittle Fracture*, in: *Advances in Applied Mechanics*, vol. 7, Elsevier, (ISSN: 0065-2156) 1962, pp. 55–129, [http://dx.doi.org/10.1016/S0065-2156\(08\)70121-2](http://dx.doi.org/10.1016/S0065-2156(08)70121-2).
- [17] M. Elices, G. Guinea, J. Gomez, J. Planas, The cohesive zone model: Advantages, limitations and challenges, *Eng. Fract. Mech.* 69 (2) (2002) 137–163, [http://dx.doi.org/10.1016/S0013-7944\(01\)00083-2](http://dx.doi.org/10.1016/S0013-7944(01)00083-2).
- [18] J. Réthoré, R.d. Borst, M.-A. Abellan, A two-scale approach for fluid flow in fractured porous media, *Internat. J. Numer. Methods Engrg.* 71 (7) (2007) 780–800, <http://dx.doi.org/10.1002/nme.1962>.
- [19] J. Réthoré, R. de Borst, M.-A. Abellan, A two-scale model for fluid flow in an unsaturated porous medium with cohesive cracks, *Comput. Mech.* (ISSN: 1432-0924) 42 (2) (2008) 227–238, <http://dx.doi.org/10.1007/s00466-007-0178-6>.
- [20] T. Mohammadnejad, A. Khoei, An extended finite element method for hydraulic fracture propagation in deformable porous media with the cohesive crack model, *Finite Elem. Anal. Des.* (ISSN: 0168-874X) 73 (2013) 77–95, <http://dx.doi.org/10.1016/j.finel.2013.05.005>.
- [21] L. De Lorenzis, T. Gerasimov, Numerical implementation of phase-field models of brittle fracture, in: *Modeling in Engineering using Innovative Numerical Methods for Solids and Fluids*, Springer, ISBN: 978-3-030-37518-8, 2020, pp. 75–101, http://dx.doi.org/10.1007/978-3-030-37518-8_3.
- [22] G. Francfort, J.-J. Marigo, Revisiting brittle fracture as an energy minimization problem, *J. Mech. Phys. Solids* (ISSN: 00225096) 46 (8) (1998) 1319–1342, [http://dx.doi.org/10.1016/S0022-5096\(98\)00034-9](http://dx.doi.org/10.1016/S0022-5096(98)00034-9).
- [23] B. Bourdin, G. Francfort, J.-J. Marigo, Numerical experiments in revisited brittle fracture, *J. Mech. Phys. Solids* (ISSN: 0022-5096) 48 (4) (2000) 797–826, [http://dx.doi.org/10.1016/S0022-5096\(99\)00028-9](http://dx.doi.org/10.1016/S0022-5096(99)00028-9).
- [24] B. Bourdin, Numerical implementation of the variational formulation for quasi-static brittle fracture, *Interfaces Free Bound.* 9 (2007) 411–430, <http://dx.doi.org/10.4171/IFB/171>.
- [25] M. Wheeler, T. Wick, W. Wollner, An augmented-Lagrangian method for the phase-field approach for pressurized fractures, *Comput. Methods Appl. Mech. Engrg.* (ISSN: 0045-7825) 271 (2014) 69–85, <http://dx.doi.org/10.1016/j.cma.2013.12.005>.
- [26] A. Mikelić, M.F. Wheeler, T. Wick, Phase-field modeling of a fluid-driven fracture in a poroelastic medium, *Comput. Geosci.* (ISSN: 1573-1499) 19 (6) (2015) 1171–1195, <http://dx.doi.org/10.1007/s10596-015-9532-5>.
- [27] A. Mikelić, M.F. Wheeler, T. Wick, A phase-field method for propagating fluid-filled fractures coupled to a surrounding porous medium, *Multiscale Model. Simul.* 13 (1) (2015) 367–398, <http://dx.doi.org/10.1137/140967118>.
- [28] A. Mikelić, M.F. Wheeler, T. Wick, A quasi-static phase-field approach to pressurized fractures, *Nonlinearity* 28 (5) (2015) 1371, <http://dx.doi.org/10.1088/0951-7715/28/5/1371>.
- [29] B. Bourdin, C. Chukwudozie, K. Yoshioka, A variational approach to the numerical simulation of hydraulic fracturing, in: *SPE Annual Technical Conference and Exhibition*, SPE–159154–MS, vol. All Days, 2012, <http://dx.doi.org/10.2118/159154-MS>.
- [30] K. Yoshioka, B. Bourdin, A variational hydraulic fracturing model coupled to a reservoir simulator, *Int. J. Rock Mech. Min. Sci.* (ISSN: 1365-1609) 88 (2016) 137–150, <http://dx.doi.org/10.1016/j.ijrmms.2016.07.020>.
- [31] C. Chukwudozie, B. Bourdin, K. Yoshioka, A variational phase-field model for hydraulic fracturing in porous media, *Comput. Methods Appl. Mech. Engrg.* 347 (2019) 957–982, <http://dx.doi.org/10.1016/j.cma.2018.12.037>.
- [32] Z.A. Wilson, C.M. Landis, Phase-field modeling of hydraulic fracture, *J. Mech. Phys. Solids* (ISSN: 0022-5096) 96 (2016) 264–290, <http://dx.doi.org/10.1016/j.jmps.2016.07.019>.
- [33] W. Ehlers, C. Luo, A phase-field approach embedded in the theory of porous media for the description of dynamic hydraulic fracturing, *Comput. Methods Appl. Mech. Engrg.* (ISSN: 0045-7825) 315 (2017) 348–368, <http://dx.doi.org/10.1016/j.cma.2016.10.045>.
- [34] S. Lee, M.F. Wheeler, T. Wick, Iterative coupling of flow, geomechanics and adaptive phase-field fracture including level-set crack width approaches, *J. Comput. Appl. Math.* 314 (2017) 40–60, <http://dx.doi.org/10.1016/j.cam.2016.10.022>.
- [35] D. Santillán, R. Juanes, L. Cueto-Felgueroso, Phase field model of fluid-driven fracture in elastic media: Immersed-fracture formulation and validation with analytical solutions, *J. Geophys. Res.: Solid Earth* 122 (4) (2017) 2565–2589, <http://dx.doi.org/10.1002/2016JB013572>.
- [36] S. Zhou, X. Zhuang, T. Rabczuk, Phase-field modeling of fluid-driven dynamic cracking in porous media, *Comput. Methods Appl. Mech. Engrg.* (ISSN: 0045-7825) 350 (2019) 169–198, <http://dx.doi.org/10.1016/j.cma.2019.03.001>.
- [37] Y. Heider, W. Sun, A phase field framework for capillary-induced fracture in unsaturated porous media: Drying-induced vs. hydraulic cracking, *Comput. Methods Appl. Mech. Engrg.* (ISSN: 0045-7825) 359 (2020) 112647, <http://dx.doi.org/10.1016/j.cma.2019.112647>.
- [38] L.-P. Yi, H. Waisman, Z.-Z. Yang, X.-G. Li, A consistent phase field model for hydraulic fracture propagation in poroelastic media, *Comput. Methods Appl. Mech. Engrg.* (ISSN: 0045-7825) 372 (2020) 113396, <http://dx.doi.org/10.1016/j.cma.2020.113396>.
- [39] A. Costa, M. Cusini, T. Jin, R. Settigast, J.E. Dolbow, A multi-resolution approach to hydraulic fracture simulation, *Int. J. Fract.* (ISSN: 1573-2673) 237 (1) (2022) 165–188, <http://dx.doi.org/10.1007/s10704-022-00662-y>.
- [40] C. Luo, L. Sanavia, L. De Lorenzis, Phase-field modeling of drying-induced cracks: Choice of coupling and study of homogeneous and localized damage, *Comput. Methods Appl. Mech. Engrg.* (ISSN: 0045-7825) 410 (2023) 115962, <http://dx.doi.org/10.1016/j.cma.2023.115962>.

- [41] T. You, K. Yoshioka, On poroelastic strain energy degradation in the variational phase-field models for hydraulic fracture, *Comput. Methods Appl. Mech. Engrg.* (ISSN: 0045-7825) 416 (2023) 116305, <http://dx.doi.org/10.1016/j.cma.2023.116305>.
- [42] T. Gerasimov, L. De Lorenzis, A line search assisted monolithic approach for phase-field computing of brittle fracture, *Comput. Methods Appl. Mech. Engrg.* (ISSN: 00457825) 312 (2016) 276–303, <http://dx.doi.org/10.1016/j.cma.2015.12.017>.
- [43] T. Heister, M.F. Wheeler, T. Wick, A primal-dual active set method and predictor-corrector mesh adaptivity for computing fracture propagation using a phase-field approach, *Comput. Methods Appl. Mech. Engrg.* (ISSN: 00457825) (2015) <http://dx.doi.org/10.1016/j.cma.2015.03.009>.
- [44] A. Sonntag, A. Wagner, W. Ehlers, Dynamic hydraulic fracturing in partially saturated porous media, *Comput. Methods Appl. Mech. Engrg.* (ISSN: 0045-7825) 414 (2023) 116121, <http://dx.doi.org/10.1016/j.cma.2023.116121>.
- [45] R. Bharali, S. Goswami, C. Anitescu, T. Rabczuk, A robust monolithic solver for phase-field fracture integrated with fracture energy based arc-length method and under-relaxation, *Comput. Methods Appl. Mech. Engrg.* (ISSN: 0045-7825) 394 (2022) 114927, <http://dx.doi.org/10.1016/j.cma.2022.114927>.
- [46] S. May, J. Vignollet, R. De Borst, A numerical assessment of phase-field models for brittle and cohesive fracture: Γ -convergence and stress oscillations, *Eur. J. Mech. A Solids* 52 (2015) 72–84, <http://dx.doi.org/10.1016/j.euromechsol.2015.02.002>.
- [47] N. Singh, C. Verhoosel, R. De Borst, E. Van Brummelen, A fracture-controlled path-following technique for phase-field modeling of brittle fracture, *Finite Elem. Anal. Des.* 113 (2016) 14–29, <http://dx.doi.org/10.1016/j.finel.2015.12.005>.
- [48] E. Börjesson, J.J.C. Remmers, M. Fagerström, A generalised path-following solver for robust analysis of material failure, *Comput. Mech.* (ISSN: 1432-0924) 70 (2) (2022) 437–450, <http://dx.doi.org/10.1007/s00466-022-02175-w>.
- [49] R.I. Borja, The analysis of consolidation by a Quasi-Newton technique, *Int. J. Numer. Anal. Methods Geomech.* 12 (2) (1988) 221–229, <http://dx.doi.org/10.1002/nag.1610120209>.
- [50] B.A. Schrefler, L. Simoni, L. Xikui, O.C. Zienkiewicz, Mechanics of partially saturated porous media, in: C.S. Desai, G. Gioda (Eds.), *Numerical Methods and Constitutive Modelling in Geomechanics*, Springer Vienna, Vienna, ISBN: 978-3-7091-2832-9, 1990, pp. 169–209, http://dx.doi.org/10.1007/978-3-7091-2832-9_2.
- [51] O.C. Zienkiewicz, A. Chan, M. Pastor, B. Schrefler, T. Shiomi, *Computational Geomechanics*, vol. 613, John Wiley & Sons, ISBN: 0-471-98285-7, 1999.
- [52] C. Miehe, F. Welschinger, M. Hofacker, Thermodynamically consistent phase-field models of fracture: Variational principles and multi-field FE implementations, *Int. J. Numer. Methods Eng.* 83 (10) (2010) 1273–1311, <http://dx.doi.org/10.1002/nme.2861>.
- [53] M.A. Biot, Mechanics of deformation and acoustic propagation in porous media, *J. Appl. Phys.* (ISSN: 0021-8979) 33 (4) (1962) 1482–1498, <http://dx.doi.org/10.1063/1.1728759>.
- [54] P.A. Witherspoon, J.S.Y. Wang, K. Iwai, J.E. Gale, Validity of cubic law for fluid flow in a deformable rock fracture, *Water Resour. Res.* 16 (6) (1980) 1016–1024, <http://dx.doi.org/10.1029/WR016i0600p01016>.
- [55] K. Yoshioka, D. Naumov, O. Kolditz, On crack opening computation in variational phase-field models for fracture, *Comput. Methods Appl. Mech. Engrg.* (ISSN: 0045-7825) 369 (2020) 113210, <http://dx.doi.org/10.1016/j.cma.2020.113210>.
- [56] C. Miehe, S. Mauthe, S. Teichtmeister, Minimization principles for the coupled problem of Darcy–Biot-type fluid transport in porous media linked to phase field modeling of fracture, *J. Mech. Phys. Solids* (ISSN: 0022-5096) 82 (2015) 186–217, <http://dx.doi.org/10.1016/j.jmps.2015.04.006>.
- [57] C. Taylor, P. Hood, A numerical solution of the Navier-Stokes equations using the finite element technique, *Comput. & Fluids* (ISSN: 0045-7930) 1 (1) (1973) 73–100, [http://dx.doi.org/10.1016/0045-7930\(73\)90027-3](http://dx.doi.org/10.1016/0045-7930(73)90027-3).
- [58] E. Oñate, J. Rojek, R.L. Taylor, O.C. Zienkiewicz, Finite calculus formulation for incompressible solids using linear triangles and tetrahedra, *Internat. J. Numer. Methods Engrg.* 59 (11) (2004) 1473–1500, <http://dx.doi.org/10.1002/nme.922>.
- [59] Stabilized mixed finite element formulations for materially nonlinear partially saturated two-phase media, *Comput. Methods Appl. Mech. Engrg.* (ISSN: 0045-7825) 195 (13) (2006) 1517–1546, <http://dx.doi.org/10.1016/j.cma.2005.05.044>.
- [60] G. Aguilar, F. Gaspar, F. Lisbona, C. Rodrigo, Numerical stabilization of Biot’s consolidation model by a perturbation on the flow equation, *Internat. J. Numer. Methods Engrg.* 75 (11) (2008) 1282–1300, <http://dx.doi.org/10.1002/nme.2295>.
- [61] J.A. White, R.I. Borja, Stabilized low-order finite elements for coupled solid-deformation/fluid-diffusion and their application to fault zone transients, *Comput. Methods Appl. Mech. Engrg.* (ISSN: 0045-7825) 197 (49) (2008) 4353–4366, <http://dx.doi.org/10.1016/j.cma.2008.05.015>.
- [62] P. Mira, M. Pastor, T. Li, X. Liu, A new stabilized enhanced strain element with equal order of interpolation for soil consolidation problems, *Comput. Methods Appl. Mech. Engrg.* (ISSN: 0045-7825) 192 (37) (2003) 4257–4277, [http://dx.doi.org/10.1016/S0045-7825\(03\)00416-X](http://dx.doi.org/10.1016/S0045-7825(03)00416-X).
- [63] W. Sun, J.T. Ostien, A.G. Salinger, A stabilized assumed deformation gradient finite element formulation for strongly coupled poromechanical simulations at finite strain, *Int. J. Numer. Anal. Methods Geomech.* 37 (16) (2013) 2755–2788, <http://dx.doi.org/10.1002/nag.2161>.
- [64] C. Gavagnin, L. Sanavia, L. De Lorenzis, Stabilized mixed formulation for phase-field computation of deviatoric fracture in elastic and poroelastic materials, *Comput. Mech.* (ISSN: 1432-0924) 65 (6) (2020) 1447–1465, <http://dx.doi.org/10.1007/s00466-020-01829-x>.
- [65] C. Miehe, M. Hofacker, F. Welschinger, A phase field model for rate-independent crack propagation: Robust algorithmic implementation based on operator splits, *Comput. Methods Appl. Mech. Engrg.* (ISSN: 00457825) 199 (45–48) (2010) 2765–2778, <http://dx.doi.org/10.1016/j.cma.2010.04.011>.
- [66] T. Gerasimov, L. De Lorenzis, On penalization in variational phase-field models of brittle fracture, *Comput. Methods Appl. Mech. Engrg.* 354 (2019) 990–1026, <http://dx.doi.org/10.1016/j.cma.2019.05.038>.
- [67] M. Hintermüller, K. Ito, K. Kunisch, The primal-dual active set strategy as a semismooth Newton method, *SIAM J. Optim.* 13 (3) (2002) 865–888, <http://dx.doi.org/10.1137/S1052623401383558>.
- [68] S. Forest, Micromorphic approach for gradient elasticity, viscoplasticity, and damage, *J. Eng. Mech.* 135 (3) (2009) 117–131, [http://dx.doi.org/10.1061/\(ASCE\)0733-9399\(2009\)135:3\(117\)](http://dx.doi.org/10.1061/(ASCE)0733-9399(2009)135:3(117)).
- [69] R. Bharali, F. Larsson, R. Jänicke, A micromorphic phase-field model for brittle and quasi-brittle fracture, *Comput. Mech.* (ISSN: 1432-0924) (2023) <http://dx.doi.org/10.1007/s00466-023-02380-1>.
- [70] R. De Borst, M.A. Crisfield, J.J. Remmers, C.V. Verhoosel, *Nonlinear Finite Element Analysis of Solids and Structures*, John Wiley & Sons, ISBN: 9781118375938, 2012, <http://dx.doi.org/10.1002/9781118375938>.
- [71] T. Wick, *Multiphysics Phase-Field Fracture: Modeling, Adaptive Discretizations, and Solvers*, vol. 28, Walter de Gruyter GmbH & Co KG, 2020, <http://dx.doi.org/10.1515/9783110497397>.
- [72] G.A. Wempner, Discrete approximations related to nonlinear theories of solids, *Int. J. Solids Struct.* (ISSN: 0020-7683) 7 (11) (1971) 1581–1599, [http://dx.doi.org/10.1016/0020-7683\(71\)90038-2](http://dx.doi.org/10.1016/0020-7683(71)90038-2).
- [73] M. Crisfield, A fast incremental/iterative solution procedure that handles “snap-through”, in: A.K. Noor, H.G. McComb (Eds.), *Computational Methods in Nonlinear Structural and Solid Mechanics*, Pergamon, ISBN: 978-0-08-027299-3, 1981, pp. 55–62, <http://dx.doi.org/10.1016/B978-0-08-027299-3.50009-1>.
- [74] M.G.D. Geers, Enhanced solution control for physically and geometrically non-linear problems. Part I—the subplane control approach, *Internat. J. Numer. Methods Engrg.* 46 (2) (1999) 177–204, [http://dx.doi.org/10.1002/\(SICI\)1097-0207\(19990920\)46:2<177::AID-NME668>3.0.CO;2-L](http://dx.doi.org/10.1002/(SICI)1097-0207(19990920)46:2<177::AID-NME668>3.0.CO;2-L).
- [75] M.G.D. Geers, Enhanced solution control for physically and geometrically non-linear problems. Part II—comparative performance analysis, *Internat. J. Numer. Methods Engrg.* 46 (2) (1999) 205–230, [http://dx.doi.org/10.1002/\(SICI\)1097-0207\(19990920\)46:2<205::AID-NME669>3.0.CO;2-S](http://dx.doi.org/10.1002/(SICI)1097-0207(19990920)46:2<205::AID-NME669>3.0.CO;2-S).
- [76] C.V. Verhoosel, J.J.C. Remmers, M.A. Gutiérrez, A dissipation-based arc-length method for robust simulation of brittle and ductile failure, *Internat. J. Numer. Methods Engrg.* 77 (9) (2009) 1290–1321, <http://dx.doi.org/10.1002/nme.2447>.
- [77] J. Vignollet, S. May, R. De Borst, C.V. Verhoosel, Phase-field models for brittle and cohesive fracture, *Meccanica* 49 (11) (2014) 2587–2601, <http://dx.doi.org/10.1007/s11012-013-9862-0>.

- [78] T. Hageman, R. de Borst, A time-based arc-length like method to remove step size effects during fracture propagation, *Internat. J. Numer. Methods Engrg.* 123 (1) (2022) 180–196, <http://dx.doi.org/10.1002/nme.6852>.
- [79] Intel, Intel oneAPI math kernel library, 2023, URL <https://www.intel.com/content/www/us/en/developer/tools/oneapi/onemkl.html>.
- [80] E. Detournay, Propagation regimes of fluid-driven fractures in impermeable rocks, *Int. J. Geomech.* 4 (1) (2004) 35–45, [http://dx.doi.org/10.1061/\(ASCE\)1532-3641\(2004\)4:1\(35\)](http://dx.doi.org/10.1061/(ASCE)1532-3641(2004)4:1(35)).
- [81] E. Detournay, D.I. Garagash, The near-tip region of a fluid-driven fracture propagating in a permeable elastic solid, *J. Fluid Mech.* 494 (2003) 1–32, <http://dx.doi.org/10.1017/S0022112003005275>.